Brush border intermicrovillar adhesion limits bacteria attachment to the small intestine brush border

Author list
Rebecca P. Cowell[1,2,†], Alexander C. Bickart[1,2,†], Suchetha R. Shashi[1,2], Alfredo Vasquez Jr.[1,2], Lee C. Brackman[1,2], Marwa A. Abdel-Dayem[3,4], Wei Chen [3], Deanna M. Bowman[5], Evan S. Krystofiak[6], Yassine Essalki[7], Isabelle Gross[7], David G. Harrison[3], Celestine N. Wanjalla[1,8], Holly M. Scott Algood[1,2,9,10], Matthew J. Tyska[6], and Leslie M. Meenderink[1,2,11,*]

[1]Division of Infectious Disease, Department of Medicine, Vanderbilt University School of Medicine, Vanderbilt University Medical Center, Nashville, TN, USA
[2]Tennessee Valley Healthcare System, Department of Veterans Affairs, Nashville, TN, USA
[3]Division of Genetic Medicine and Clinical Pharmacology, Department of Medicine, Vanderbilt University Medical Center, Nashville, TN, USA
[4]Department of Biochemistry and Pharmacology, Faculty of Pharmacy, Horus University-Egypt, New Damietta 34518, Egypt
[5]College of Graduate Studies, Northeast Ohio Medical School, Rootstown, OH, USA
[6]Department of Cell and Developmental Biology, Vanderbilt University School of Medicine, Nashville, TN, USA
[7]Regenerative Nanomedicine, INSERM UMR 1260, University of Strasbourg, CRBS, FMTS, Strasbourg, France
[8]Tennessee Center for AIDS Research, Vanderbilt University Medical Center, Nashville, TN, USA
[9]Department of Pathology, Microbiology and Immunology, Vanderbilt University School of Medicine, Vanderbilt University Medical Center, Nashville, TN, USA
[10]Vanderbilt Institute of Infection, Immunity, and Inflammation (VI4), Vanderbilt University Medical Center, Nashville, TN, USA

[11]Lead Contact
*Correspondence: leslie.meenderink@vumc.org
[†]Co-first authors.

SUMMARY
Enterocytes present a continuous array of uniform, tightly packed, apical microvilli known as the “brush border”. Adjacent microvilli tips are linked by an intermicrovillar adhesion complex (IMAC) composed of cadherins that are required for microvillar packing, length uniformity, and junctional integrity, with disruption linked to intestinal autoimmune disease and infections. We found that IMAC-deficient mice have increased adherent (actin-dependent) and mucosal (actin-independent) bacteria in the terminal ileum. These bacteria are primarily commensals without differences in diversity between groups. Initial segments of Segmented filamentous bacteria (SFB) recruit microvilli proteins (EPS8/IRTKS) and Arp2/3 to remodel actin. SFB anchor contiguous to cell junctions and incorporate ZO-1 into their attachments. Together, these data reveal maturation of the SFB host-microbe interface that mirrors the complex SFB lifecycle. Our work indicates a previously unrecognized role for the brush border as a key component of host defense against luminal microbes.

Keywords (up to 10)
microvilli, brush border, IMAC, CDHR2, CDHR5, intermicrovillar adhesion, ileum, mucosal bacteria, segmented filamentous bacteria

Tissue-associated = ALL
Adherent = actin-dependent
Mucosal = actin-independent

INTRODUCTION

The small intestine is essential for life, serving as the sole site of nutrient absorption. The intestinal epithelium consists of a continuous layer of cells including enterocytes, goblet cells, tuft cells, and enteroendocrine cells, with enterocytes being most abundant. The surface of the small intestine is organized into finger-like tissue folds (villi), while individual enterocytes display membrane protrusions (microvilli), at their apical surface to increase the surface area and optimize nutrient absorption. Stem cells housed in crypts at the base of the villi continuously generate new enterocytes. Mature enterocytes emerge from crypts onto the villus, collectively migrate toward the villus tips[1], and are ultimately shed into the lumen resulting in turnover of the epithelium every ~3-5 days[2]. The apical surface of each enterocyte contains thousands of uniform, tightly-packed microvilli, known as the brush border. Intermicrovillar adhesion complexes (IMACs) link the tips of adjacent microvilli to maintain dense packing and consistent microvillus length[3, 4]. Several studies implicate IMAC disruption in chronic intestinal inflammatory disease as a potential precursor indicative of underlying epithelial defects or as a response to chronic inflammation, damage, or dysbiosis[5-9]. Understanding how IMAC dysfunction shapes the mucosal environment at the epithelial surface will help clarify fundamental mechanisms of intestinal homeostasis and disease.

Each microvillus consists of a membrane-wrapped core of 20-40 parallel actin filaments (F-actin)[10, 11]. The actin cores extend “rootlets” into the sub-apical terminal web where microvilli are anchored and non-muscle myosin 2C (MYH4) regulates microvillus length and apical tension[10, 12-14]. The distal tip of the actin core is embedded in an electron-dense tip complex comprised of EPS8 and IRTKS[15-18]. These factors are essential for initiating microvillus growth and maintaining the stability of immature microvilli[17]. The microvillus F-actin core is organized by actin-bundling proteins villin-1 (VIL1)[19], Espin (ESPN)[20], Fimbrin (also known as Plastin, PLS1)[21], and mitotic interactor and substrate of PLK1 (MISP)[22]. Actin-membrane linkers (MYO1A[23], MYO1D[24], MYO6[25], and EZRIN family proteins[26]) ensure plasma membrane wrapping of each microvillus. Intermicrovillar adhesion complexes (IMACs) link the tips of adjacent microvilli to maintain dense packing and consistent microvillus length[3, 4]. A basal immunoglobulin link (TMIGD1, EBP50, and E3KARP)[27] is also important for microvillar packing and supports membrane wrapping via EZRIN.

The IMACs bridge adjacent microvilli via trans-heterophilic CDHR2 (Cadherin-related family protein member 2, also known as protocadherin-24)/CDHR5 (Cadherin-related family member 5, also known as mucin-like protocadherin) extracellular linkages[4]. The CDHR2/CDHR5 intracellular domains connect to the F-actin core via protein scaffolds (USH1C, ANKS4B) and the myosin motor/light chain (MYO7B/CALML) (Figure 1A)[4, 28-32] which also transports the complex to the tips of microvilli (Figure 1A, green arrow)[33]. Of note, loss of any one IMAC component disrupts IMAC function and prevents tip localization. During differentiation, tip-links stabilize adjacent microvilli as the brush border progressively fills the apical surface[4, 12, 34]. In mature enterocytes, the IMAC maintains hexagonal microvilli packing and uniform microvilli length[4, 28, 35, 36]. Notably, the IMAC not only connects microvilli within a single enterocyte, but also

microvilli on adjacent enterocytes[34] creating a continuous luminal brush border. IMAC disruption results in junctional defects with reduced localization of junctional proteins, loss of normal apical tension, and decreased *in vitro* transepithelial electrical resistance (TEER)[34, 35, 37]. Brush border formation is robust with significant functional redundancy; remarkably, a triple knockout (KO) mouse with deletion of three microvillus bundling proteins (VIL1, ESPN, PLS1) is viable and retains the ability to make microvilli[38]. Typically, knockout mice with defects in microvilli ultrastructure and organization are viable and relatively healthy at baseline with deficits (tissue fragility[39], increased sensitivity to DSS[36, 39, 40]) revealed only under stress. Mice lacking the IMAC component, CDHR5, have increased sensitivity to DSS including elevated levels of bacteria invading the colonic mucosa compared to wildtype (WT) mice[36].

Defects in microvilli structure have been linked to intestinal autoimmune disease including Celiac Disease[5] and inflammatory bowel disease (IBD)—comprised of Crohn's Disease[6] and Ulcerative Colitis[36]; whether the structural defects are a cause or consequence of disease remains unclear. IBD is thought to arise from an inappropriate inflammatory response to gut microbes in genetically susceptible hosts, further modified by environmental factors including dysbiosis[7, 8]. VanDussen et al. (2018) found that expression of genes critical for microvilli organization, including the IMAC (CDHR2, CDHR5, USH1C, ANSK4B and MYO7B), were decreased in intestinal samples from patients with Crohn's Disease even in the absence of active inflammation[6]. Identification of 'short microvilli' in patients with Crohn's Disease has been proposed as a potential biomarker to predict non-response to biologic therapies[9]. Single cell RNA sequencing from patients with Ulcerative Colitis demonstrated CDHR5 is downregulated in inflamed areas[36]. These studies implicate IMAC disruption in chronic intestinal inflammatory disease as a potential precursor indicative of underlying epithelial defects or as a response to chronic inflammation, damage, or dysbiosis.

The small intestine serves as a defensive barrier to microbes and toxins that reside within the intestinal lumen[41]. The brush border is the first point of contact between the intestinal epithelium and luminal microbes with the densely packed microvilli preventing bacterial attachment and internalization[42]. Numerous bacteria remodel the actin cytoskeleton exploiting the host cell environment to support attachment and reproduction, including canonical intestinal pathogens *Listeria monocytogenes*[43-47], enteropathogenic *Escherichia coli* (EPEC)[48], enterohemorrhagic *Escherichia coli* (EHEC)[48], and *Salmonella typhimurium*[49-53]. While there is a significant body of work describing how pathogenic bacteria repurpose the host cytoskeleton to support infection, very little is known about commensal interactions with the epithelial surface. We sought to understand how defects in brush border organization alter host-microbe interactions at the surface of the small intestine.

Results

Mice with a disrupted IMAC have increased adherent bacteria in the terminal ileum. To understand how disruptions in microvilli packing and organization alter small intestinal physiology *in vivo*, we examined the terminal ileum of mice with and without tissue-specific disruption of intermicrovillar adhesion. *Cdhr2*$^{fl/fl}$ mice express full-length Cdhr2 but harbor a conditional deletion allele that, when crossed with villin-Cre expressing mice, results in tissue-specific deletion of exons 4 and 5, leading to a deletion of Cdhr2 in intestinal crypts and epithelium referred to herein as *Cdhr2*$^{\Delta epi}$ (Supplemental Figure S1A and previously described[35]). Whole mount scanning electron microscopy (SEM) of the terminal ileum revealed a striking population of filamentous bacteria adherent to the epithelial surface in *Cdhr2*$^{\Delta epi}$ mice, with bacteria concentrated distally on villi (Figure 1C). By contrast, *Cdhr2*$^{fl/fl}$ control mice had few if any visible adherent bacterial filaments (Figure 1B). To determine if the increase in adherent bacteria was specific to *Cdhr2*$^{\Delta epi}$ mice, we examined terminal ileum tissue from mice lacking an alternate IMAC component, Cdhr5. We again observed a dramatic increase in adherent filamentous bacteria in the ileum of Cdhr5 KO mice compared to WT control mice (Figure 1D-E). Cdhr5 WT control mice had minimal adherent filamentous bacteria (Figure 1D, zoom). Based on similar results from two separate KO mice that disrupt intermicrovillar adhesion and brush border organization, we conclude that loss of IMAC function, due to loss of Cdhr2/5, facilitates bacterial adhesion to the epithelial surface and augmented colonization of the terminal ileum. Moving forward, our studies focused on the *Cdhr2*$^{fl/fl}$ and *Cdhr2*$^{\Delta epi}$ mice as the tissue specific deletion allows us to focus on the role of the intestinal epithelium. Additionally, we used paired *Cdhr2*$^{fl/fl}$ and *Cdhr2*$^{\Delta epi}$ littermates generated from maternal *Cdhr2*$^{\Delta epi}$ and paternal *Cdhr2*$^{fl/fl}$ mice (Supplemental Figure 1B) to generate consistent microbial exposure for littermates from birth through weaning.

Mice with a disrupted IMAC have multiple populations of adherent bacteria enriched in the terminal ileum. The SEM whole mount studies **(**Figure 1B and 1C), while qualitatively dramatic, posed a quantification challenge due to the dense and overlapping bacteria, as well as non-uniformity in visualizing bacterial attachments in three-dimensional (3D) tissue. To quantify adherent bacteria, we used laser scanning confocal microscopy (LSCM) of whole mount tissue followed by 3D reconstruction of the villus surface. DAPI (4′,6-diamidino-2-phenylindole) was used to mark both epithelial cell nuclear DNA and bacterial DNA (Figure 2A). To facilitate visualization of bacteria, DAPI images were segmented, viewed in separate channels, and differentially contrasted (Figure 2B). Whole mount tissue was co-stained with phalloidin (F-actin), highlighting the sites of bacterial attachment to the brush border (Figure 2C, white arrowheads). *Cdhr2*$^{\Delta epi}$ mouse ileum contained significantly more bacterial attachments (Figure 2G). The F-actin attachments colocalized with chains of bacterial DNA, consistent with the filaments seen by SEM. However, whole mount confocal imaging revealed an additional population of adherent single bacteria (Figure 2D), which were also enriched in *Cdhr2*$^{\Delta epi}$ mouse ileum (Figure 2I). Given that adherent bacteria often target and disrupt microvilli[54-59],we assessed the localization of brush border actin-binding proteins, to characterize the adherent bacteria. Epidermal growth factor pathway substrate 8

(EPS8) is a microvillus tip protein that binds actin barbed ends and is essential for microvilli formation and stability[17, 18, 60, 61]. In *Cdhr2*$^{fl/fl}$ and *Cdhr2*$^{\Delta epi}$ mice, EPS8 localized to only a subset of adherent bacteria (Figure 2E-F, white arrowheads). While present in both *Cdhr2*$^{fl/fl}$ and *Cdhr2*$^{\Delta epi}$ mice, EPS8-containing attachments were significantly increased in *Cdhr2*$^{\Delta epi}$ mice (Figure 2H) particularly within single bacteria (Figure 2J). However, most adherent bacteria were filamentous and lacked EPS8 staining (Figure 2G, K).

Given the increased level of adherent bacteria in *Cdhr2*$^{\Delta epi}$ mice, we evaluated the ileum for signs of inflammation. Hematoxylin and eosin (H&E) staining of the small intestine did not reveal evidence of tissue damage or increased immune infiltrates (data not shown). We used qRT-PCR to quantify the expression of inflammatory genes commonly elevated in bacterial infections including the chemokine *Cxcl1*, cytokines (*Il22, Il17a,* and *Il6)*, and the bactericidal antimicrobial peptide *Reg3g*. There were no differences between *Cdhr2*$^{fl/fl}$ and *Cdhr2*$^{\Delta epi}$ mice (Supplemental Figure 1C). We also performed flow cytometry to phenotype the lymphocytes in the lamina propria of the small intestine (Supplemental Figure 1F), mesenteric lymph nodes (data not shown), and inguinal lymph nodes (data not shown) from age- and sex-matched *Cdhr2*$^{\Delta epi}$ and *Cdhr2*$^{fl/fl}$ littermates. Representative plots of the gating scheme used to identify T cell subsets and IL-17A and IFN-γ expressing cells are shown (Supplemental Figure 1D and E, respectively). T cell subsets (CD4, CD8, and gamma-delta ($\gamma\delta$)) were not significantly different in the lamina propria (Supplemental Figure 1F). Further, the percentage of interferon-gamma (IFN-γ) and IL-17A-producing cells in these T cell subsets did not differ (Supplemental Figure 3G). There was a trend towards higher IL-17A expression in gamma-delta ($\gamma\delta$) T cells in the mesenteric lymph nodes of *Cdhr2*$^{\Delta epi}$ mice but this was not significant (data not shown). Overall, this indicates that while *Cdhr2*$^{\Delta epi}$ mice have higher numbers of bacteria in contact with the intestinal epithelium including formation of F-actin based attachments, the mice are not mounting an enhanced systemic or tissue-resident inflammatory response.

Loss of intermicrovillar adhesion facilitates polymicrobial tissue colonization with bacteria utilizing actin-dependent and actin-independent surface attachments. To understand if loss of intermicrovillar adhesion results in colonization with specific bacteria, we sought to identify the ileum-associated bacteria in *Cdhr2*$^{fl/fl}$ and *Cdhr2*$^{\Delta epi}$ mice. The filamentous bacteria morphology observed by SEM and whole mount imaging are suggestive of *Candidatus Arthromitis*, also known as segmented filamentous bacteria (SFB) which preferentially colonize the mouse ileum shortly after weaning then decline to very low levels over several weeks[62, 63]. We performed fluorescence *in situ* hybridization (FISH) directed against SFB 16s rRNA (SFB FISH)[64-66]. Filamentous bacteria on sectioned ileum from *Cdhr2*$^{\Delta epi}$ mice stained with the SFB FISH probe (Figure 3A). While whole mount *Cdhr2*$^{fl/fl}$ mouse ileum demonstrated low levels of adherent bacteria, the low density of adherent bacteria consistently resulted in sectioned tissue with no tissue-associated bacteria limiting analysis (data not shown). Staining *Cdhr2*$^{\Delta epi}$ ileum for actin, DNA, and SFB FISH confirmed SFB directly contacts

the F-actin rich brush border (Figure 3B, zoom 1, arrowhead). Together these data establish that the adherent filaments in *Cdhr2*$^{\Delta epi}$ mice are SFB (Figures 1C and 2).

Non-SFB bacteria were also identified in contact with the epithelial surface, but they lacked the F-actin attachments seen in Figure 2. We identified clusters of bacteria and scattered individual bacteria consistently associated with SFB (Figure 3B, zoom 2, asterisk; Figure 4F, zoom 3). 3D volume reconstruction demonstrated bacteria associated with villus goblet cells (Figure 3C zoom). Actin staining (magenta) delineates the brush border, and EPS8 (green) marks the distal tips of microvilli. Goblet cells are visible as gaps in the apical brush border associated with a cytoplasmic void where mucus is stored or was recently secreted (Figure 3C, Supplemental Figure 2A). Standard immunofluorescence (IF) and EM tissue processing consistently preserves the apical mucus associated with goblet cells as seen on SEM (Figure 1A and C; Supplemental Figure 2B, cyan overlay). Bacteria are observed in direct contact with goblet cells—typically at the cell periphery (Figure 3C zoom, white arrowheads) or in the adjacent lumen—suggestive of mucus binding (Figure 3C zoom, orange arrowheads). An oblique view more clearly highlights three goblet cells with associated bacteria (Supplemental Figure 2C), white and orange arrowheads indicate goblet cell- and mucus-associated bacteria, respectively). Viewed as separate channels, bacteria are again seen at the goblet cell surface (Figure 3D, Supplemental Figure 2D). These bacteria do not stain with the SFB FISH probe (Figure 3E). Additionally, tissue-associated bacteria were seen in large groups overlying the epithelial surface (Figure 3F). Zoom images revealed layered colonies of bacteria (Figure 3F, zooms 1-2, white arrowheads). They do not utilize F-actin attachments; rather the bacteria are closely apposed to the brush border, mirroring but not disrupting the surface F-actin (Supplemental Figure 3A). To visualize the relationship between bacteria and the epithelial surface, Imaris was used to generate 3D surfaces representing brush border actin (magenta) and surface bacteria (orange) (Supplemental Figure 3B-C). The bacteria establish a complex, multi-layered structure extending along the epithelium (at least 25 x 4 μm in xy and 4 μm in z, Supplemental Figure 3B), consistent with biofilm formation (Figure 3F, zoom 1-2). Rotational views of the bacteria and actin surfaces highlight the 3D structure of the bacterial colony (Supplemental Figure 3B). Moreover, the bacteria consistently lie above the actin which maintains a smooth, continuous surface (Supplemental Figure 3C). Like goblet cell-associated bacteria, these bacteria do not stain with the SFB FISH probe (Supplemental Figure 3D). Together, these data show IMAC disruption allows multiple populations of bacteria to colonize the epithelial surface. Moreover, bacteria employ multiple attachment methods including anchoring to epithelial cells utilizing F-actin, colonization of adherent bacteria, mucus-binding, and surface colony/biofilm formation.

While the adherent filamentous bacteria colonizing the terminal ileum are identified as SFB, the other mucosal-associated bacteria remain unknown. We used shotgun metagenomic sequencing to identify mucosal bacteria and to assess for microbial shifts in *Cdhr2*$^{\Delta epi}$ mice compared to *Cdhr2*$^{fl/fl}$ mice. Paired sets of *Cdhr2*$^{fl/fl}$ and *Cdhr2*$^{\Delta epi}$

littermates were initially co-housed to establish consistent maternal microbial exposure, then separated by genotype at weaning (Figure 3G). Stool was collected immediately prior to separation, and stool and ileum tissue were collected between 5 and 8 weeks of age. Relative abundance of bacterial phyla shown as stacked bar graphs (Figure 3H). There were no significant differences in alpha diversity using either the Simpson's Diversity Index or the Berger-Parker Dominance Index (Figure 3I). Beta diversity calculations were not completed due to the high level of variation in read count. These data confirm polymicrobial bacteria associate with ileum tissue, dominated by commensals, but opportunistic pathogens, pro-inflammatory bacteria, and potential pathogens were also detected (Figure 3J). Plant bacteria were detected in all samples and were thought to be most likely due to residual food/luminal contents. Environmental bacteria were detected in only a few samples and were considered insignificant or attributed to trace contamination. Neither the stool nor the tissue-associated bacteria showed a marked difference between *Cdhr2*$^{fl/fl}$ and *Cdhr2*$^{\Delta epi}$ mice. Overall, the most abundant bacteria identified in both groups of mice were SFB (consistent with confirmatory FISH staining) and *Lactobacillus murinus*; both known to colonize the small intestine. Many commensals including *Lactobacillus*, do not adhere directly to the epithelial surface, and are thought to attach to the overlying mucus or extracellular matrix[67, 68] consistent with the patterns seen in non-SFB bacteria associated at the epithelial surface (Figure 3C-F). Overall, these data demonstrate that disruption of IMAC function allows bacteria to encroach on the epithelial surface without markedly changing the luminal microbiome composition.

Adherent primary SFB segments recruit microvilli tip proteins (EPS8 and IRTKS) and remodel the actin cytoskeleton via Arp2/3. Using confocal imaging, we identified two distinct groups of bacteria intimately bound to the epithelial surface via F-actin attachments: filamentous bacteria identified as SFB, and single bacteria co-localized with EPS8 that remain unidentified. Microbiome analysis did not provide obvious candidate bacteria known to utilize F-actin attachments, other than SFB. Given that brush border microvilli are the first point of epithelial cell contact for luminal bacteria, we hypothesized that single adherent bacteria with EPS8 target microvillar proteins to facilitate actin remodeling. To test this idea, we used an immunostaining approach to define the molecular composition of the bacterial attachments. We focused on *Cdhr2*$^{\Delta epi}$ mice which have significantly more adherent bacteria than *Cdhr2*$^{fl/fl}$ mice overall, including 4-fold more bacteria with F-actin/EPS8 attachments (Figure 2H). The level of mucosal bacteria was evident in low magnification images of DNA staining at the villus surface (Figure 4A-E). Z-depth color-coding highlights the 3D nature of the adherent bacteria with progressive color change indicating the bacteria extend across multiple confocal image planes (Figure 4B). In enterocytes, EPS8 is normally localized to the tips of microvilli (Figure 4A, zoom 1, white arrowheads; also seen in Figure 3C-D). However, EPS8 also localizes to a subset of adherent bacteria (Figure 2E-F). Areas of moderate bacteria density were assessed at high magnification to allow clear identification of single versus filamentous bacteria associated with attachment sites. EPS8 colocalized only with single bacteria (Figure 4A, zooms 1-3, yellow overlay). Adjacent filaments lacked EPS8 signal (Figure 4A, zooms 1-3, blue overlay). Strikingly,

the EPS8 staining at times adopts a teardrop shape (Figure 4A, zooms 1-2, black arrowheads), reminiscent of SFB holdfast segments (the first segment of SFB that attaches to the epithelium)[69].

Next, we assessed the localization of IRTKS (insulin receptor tyrosine kinase substrate, also known as brain-specific angiogenesis inhibitor a-associated protein 2-like protein 1—BAIAP2L1), a member of the microvillus tip complex and an EPS8 binding partner[18, 70]. IRTKS is an I-BAR (inverse-bin-amphiphysin-Rvs) protein[71-73]. I-BAR domains function to sense and induce membrane curvature[70]. IRTKS also contains an SH3 domain to recruit signaling partners and a WH2 domain that binds actin monomers. Ultimately, I-BAR proteins like IRTKS provide a functional link between changes in membrane structure and remodeling of the underlying actin cytoskeleton[18]. Within enterocytes, IRTKS localizes to the distal tips of actively growing microvilli, recruiting EPS8, and promoting microvilli growth[12, 17, 18]. In the mature brush border IRTKS localizes along the length of microvilli (Figure 4B, zoom 1)[12, 17, 18]. Of note, EHEC, hijacks IRTKS to generate actin rich “pedestals” used to attach to the epithelium. We identified IRTKS enriched at the surface of single adherent bacteria, best visualized when captured in cross section in the xy-imaging plane (Figure 4B, zoom 2, inset). In contrast, adherent SFB filaments contained faint IRTKS colocalized with the F-actin attachment site, (Figure 4B, zoom 3, inset) and more prominently in a ring where the embedded holdfast segment touches the cell surface, but lacked the surface localization seen in single bacteria. These data demonstrate the EPS8-positive adherent bacteria recruit microvilli tip proteins associated with actin remodeling to their sites of attachment.

Given adherent single bacteria recruit microvillar tip proteins (EPS8/IRTKS), we sought to determine whether the bacteria directly incorporate F-actin from microvilli into their attachment sites. Cellular arrays of F-actin are made from either parallel bundles (e.g. microvilli) or branched filaments (e.g. adherens junctions) and can be rapidly remodeled. The actin structure is defined by actin-binding proteins and the actin nucleator used to create new filaments. To define the F-actin structure within bacterial attachments, we used immunostaining to assess presence of proteins characteristic of each type of actin array. VIL1 and ESPN are bundling proteins that maintain the parallel F-actin bundles in each microvillus core[19, 20]. VIL1 was not enriched at single bacteria attachments (Figure 4C, zoom 2). VIL1 was occasionally seen at filamentous SFB attachment sites (Figure 4C, zoom 1, black arrowhead) but more consistently was not present at filamentous SFB attachments (Figure 4C, zoom 1). In contrast, ESPN consistently colocalized with F-actin attachments of both single bacteria and SFB filaments (Figure 4D, zooms 1-2). However, ESPN intensity was markedly lower than within the brush border. These results do not support bundled, parallel F-actin as the primary structure underlying bacterial attachments. Given the paucity of bundling proteins within bacterial attachment sites, we assessed markers of branched actin. The Arp2/3 complex, comprised of seven protein subunits, is the primary nucleator of

branched actin[74]. We stained for ACTR3 (actin related protein 3, Arp3), a subunit of the Arp2/3 complex. ACTR3 localized to adherent single bacteria but not to adherent SFB filaments (Figure 4E, zooms 1-2), mirroring the pattern seen with EPS8. Based on these data, we conclude that adherent single bacteria recruit EPS8/IRTKS to facilitate actin remodeling and not to incorporate bundled microvilli F-actin. Positive ACTR3 immunostaining at single adherent bacteria indicates that the bacteria are actively remodeling the actin cytoskeleton. Higher magnification SEM images of *Cdhr2*$^{\Delta epi}$ ileum show single adherent bacteria mixed with filamentous bacteria (Figure 4G). Of note, elongated microvilli were seen at the base of some SFB filaments which could account for the inconsistent detection of VIL1 at the edge of SFB filament attachments (Figure 4G, zooms 1-4).

EPS8 and Arp2/3 consistently localized to single bacteria with actin-dependent attachment sites while SFB filaments lacked both markers. Additionally, EPS8 positive bacteria bore striking morphological similarity to primary SFB segments, e.g. teardrop shape that tapers to a point in the attachment. Given this, we hypothesized adherent EPS8 positive bacteria represented an early step in SFB attachment (e.g. initial attachment of the holdfast segment). Using whole mount tissue for immunofluorescence facilitates visualization of greater numbers of actin-dependent adherent bacteria; however, whole mount tissue is not optimal for FISH. To increase likelihood of visualizing single bacteria on paraffin tissue sections, we processed thicker (10-15 μm) serial sections from each sample. The number of EPS8/F-actin attachments per section ranged from zero to three. Tissue sections were co-stained for DAPI, SFB FISH (SFB), actin, and EPS8. MaxIP of segmented bacterial DNA and actin viewed with dual z-depth color-coding affirmed the presence of multiple populations of ileum-associated bacteria (Figure 4F). Single bacteria and filamentous bacteria contact the epithelial surface (Figure 4F, zoom 1). Filamentous bacteria are visualized nearing the brush border but are transected by the sectioning plane before contacting the cell surface (Figure 4F, zoom 2). Finally, groups of bacteria are clustered around filamentous bacteria (Figure 4F, zoom 3). Intensity color-coded, maxIP of the SFB FISH channel (SFB) colocalized with filamentous bacteria including short chains (Figure 4F, zooms 1-3), but also with a single bacterium at the cell surface (Figure 4F, zoom 1 boxed area and zoom 4). Of note, additional single bacteria at the cell surface do not colocalize with SFB FISH (Figure 4F, zoom 4, white arrowheads), nor do the bacteria clustered around the SFB filament (Figure 4F, zoom 3) which serve as internal controls. Finally, the SFB positive single bacterium lies at least 4 μm from either end of the tissue section limiting the chance that it appears to be a “single” bacterium as an artifact of tissue sectioning. The single SFB bacterium is in contact with the F-actin surface and colocalizes with EPS8 (Figure 4F, zoom 4), consistent with the previously identified population of EPS8 positive adherent bacteria. These data indicate SFB primary segments recruit EPS8/IRTKS and Arp2/3 to remodel surface actin generating their distinctive actin-dependent “holdfast” points. The mature SFB filaments lack these molecular markers of actin remodeling.

SFB actin-dependent attachments incorporate ZO-1 in continuity with junctional complexes. Previous studies established CDHR2 knockout results in cell-cell junction

defects including reduced localization of junctional proteins (tight junctions: ZO-1 and Claudin-7; adherens junctions: E-cadherin and β-catenin) and decreased MYH4, suggestive of lower junctional tension[35, 37]. In addition to brush border defects, *Cdhr2*$^{\Delta epi}$ mice have abnormal tissue morphology with uneven epithelial surfaces and apically "domed" enterocytes[35]. Minimal differences are apparent at low magnification (Figure 5A); however, as previously reported[35], higher magnification images reveal defects. Despite consistent processing methods, *Cdhr2*$^{\Delta epi}$ villi frequently showed damage and cell loss at the tips not seen on *Cdhr2*$^{fl/fl}$ villi—suggestive of increased tissue fragility. Structural defects are visible throughout the villus but are most pronounced at villus tips (Figure 5A, zooms 1-4), including brush border discontinuity at cell-cell junctions (Figure 5B).

Given high levels of adherent SFB in Cdhr2$^{\Delta epi}$ ileum and that SFB are known to anchor preferentially near cell-cell junctions[63], we hypothesized SFB target junctions for attachment. Using whole mount tissue, we quantified the distance from the center of adherent bacteria to the closest cell-cell junction. SFB anchored closer to cell-cell junctions on *Cdhr2*$^{\Delta epi}$ ileum compared to *Cdhr2*$^{fl/fl}$ ileum (median distance of 1.22 μm and 1.56 μm, respectively; Figure 5C). The subset of SFB colocalized with EPS8 (representing initial SFB segments) also anchored closer to cell-cell junctions on *Cdhr2*$^{\Delta epi}$ ileum compared to *Cdhr2*$^{fl/fl}$ ileum (median 0.99 μm v. 1.41 μm, respectively; Figure 5C).

Little is known about the molecular composition of SFB attachments beyond the utilization of F-actin[75]. Given the proximity of adherent SFB to cell-cell junctions is enhanced when intermicrovillar adhesions are disrupted via CDHR2 deletion, we sought to determine whether SFB attachments target junctional proteins. To test this idea, we used an immunostaining approach to assess the localization of junctional proteins relative to adherent bacteria. Frozen tissue sections were stained for DNA (DAPI, segmented as previously described to visualize cellular nuclei and bacteria), F-actin (phalloidin), ZO-1 (tight junctions), and E-cadherin (adherens junctions). Confocal imaging of *Cdhr2*$^{\Delta epi}$ ileum revealed ZO-1 localized to bacterial attachment sites. In enterocytes, ZO-1 encircles the lateral edge of the cell just below the brush border forming an adhesive belt between adjacent cells (Figure 5D, zoom 1). When bacterial attachments are sectioned parallel to the cell surface, the actin-rich attachment is seen as an open ring of F-actin that tapers deeper into the cell (Figure 5D, zoom 2). ZO-1 localizes inside the F-actin ring (between the bacterial DNA and F-actin) while E-cadherin is not enriched at attachment sites. When sectioned longitudinally, the bacterial attachment is seen as a defect in the brush border with a teardrop shaped F-actin attachment extending into the cell (Figure 5D, zoom 3). ZO-1 is concentrated where the bacterium meets the cell surface. An oblique section parallel to a representative bacterial filament as it meets the cell surface more clearly shows ZO-1 encircling the primary SFB segment (Figure 5E-F) with the ZO-1 surrounding the bacterium in continuity with ZO-1 in adjacent cell-cell junctions (Figure 5F-G). ZO-1 forms a layer between the surface bacterium which remains extracellular and the deeper F-actin attachment (Figure 5H).

DISCUSSION

CDHR2 is a core component of the IMAC. The original studies characterizing *Cdhr2*$^{\Delta epi}$ mice demonstrated profound ultrastructural brush border defects (short, disorganized microvilli with decreased packing density) and reduced localization of multiple apical markers[35]. Despite these ultrastructural defects, the mice appeared healthy. Thus, the *Cdhr2*$^{\Delta epi}$ mouse model provided an opportunity to study how brush border disruption influences host defense *in vivo*. Our work focused on the terminal ileum as it houses the core of the intestinal immune system and has the highest bacterial concentration in the small intestine. Investigating SEM images from *Cdhr2*$^{\Delta epi}$ mice showed striking basal colonization with adherent, filamentous bacteria compared to control *Cdhr2*$^{fl/fl}$ mice. These findings were confirmed in another IMAC-deficient model, *Cdhr5* KO mice. While *Cdhr5* KO mice were also reported to have shorter, less densely-packed microvilli and increased sensitivity to Dextran Sodium Sulfate (DSS)-induced colitis (including increased tissue invasive bacteria) compared to *Cdhr5* WT mice[36], we also observed small intestine defects in the absence of stressors in *Cdhr5* KO mice, similar to those observed in the *Cdhr2*$^{\Delta epi}$ mouse model. The dense inner mucus layer that separates the colonic epithelium from luminal bacteria[76, 77], may account for this difference. Epithelial damage and inflammation in DSS colitis are preceded by increased permeability of the inner mucus layer, allowing luminal bacteria to gain access to the epithelial surface[78, 79]. In the absence of damage, the dense colonic mucus layer appears sufficient to compensate for the underlying epithelial defects in the colon of CDHR5-deficient mice[36]. In contrast, the small intestine mucus is less dense and only loosely associated with the epithelial surface[80], providing less robust protection from luminal bacteria. Thus, loss of IMAC tip links in the small intestine is sufficient to allow luminal bacteria to attach to the epithelial surface, resulting in more adherent bacteria in the terminal ileum of *Cdhr2*$^{\Delta epi}$ and *Cdhr5* KO mice in the absence of stressors.

Most bacteria utilizing actin-based attachments are pathogens[48, 81, 82]. However, given the lack of infectious symptoms (e.g. weight loss or diarrhea), localization in the terminal ileum, and the characteristic tear-drop shape of the actin attachments, the commensal SFB was a prime candidate for the adherent bacteria—confirmed using FISH. We anticipated non-SFB commensals identified on sequencing were due to the presence of residual luminal bacteria from incompletely washed tissue. However, paraffin-embedded tissue sections (which undergo less harsh washing/processing compared to SEM and whole mount tissue) revealed not only SFB but also non-SFB bacteria directly interacting with the epithelial surface of *Cdhr2*$^{\Delta epi}$ mice. Non-SFB bacteria employ multiple actin-independent mechanisms to associate with the mucosal surface including sub-colonization of SFB[63], mucus binding at the surface[83-85], and biofilm formation[86, 87]. While these bacteria are most likely commensals, validated FISH probes have not been established for most commensal species to allow direct visual confirmation via FISH. Colonization of the epithelium with bacteria utilizing diverse attachments indicates intermicrovillar adhesion globally contributes to the basal separation between luminal bacteria and the small intestine epithelium—not only to defense against pathogens.

Normally, commensals in the ileum do not have direct contact with the epithelium and live in suspension[88]. In our study, we observed bacteria in direct contact with the epithelium without marked changes in the composition of the microbiota of *Cdhr2*$^{\Delta epi}$ mice. Previous studies of *Cdhr5* KO mice also did not show changes in the microbiota compared to *Cdhr5* WT mice[36]. Bacterial access to the epithelial surface is likely due to the disruption of the IMAC via loss of CDHR2 and the resulting splayed, less densely packed microvilli. Microvilli packing density is a critical physical barrier to prevent bacterial attachment. Mice lacking the IMAC component CDHR2, have a ~30% reduction in microvilli density and microvilli are less ordered suggestive of "liquid" packing rather than the tight hexagonal packing typical of brush border microvilli[35]. Additionally, IMAC disruption causes apical doming which combined with reduced microvillar density may present easier targets for bacterial adhesion with greater access to the lateral microvillar membrane surfaces as well as the cell surface in the intermicrovillar spaces. The lack of change in the microbiota composition differs from other components of host defense such as antimicrobial peptides where defects result in altered microbial composition[66]. Dysbiosis broadly encompasses any imbalance in the equilibrium between beneficial and potentially harmful microbiota in the gut including loss of beneficial bacteria, excess growth of potentially pathogenic bacteria, loss of overall diversity, or changes in local distribution of bacteria[89]. Unlike the classical conception of dysbiosis as a shift in bacteria populations that make up the microbiota, *Cdhr2*$^{\Delta epi}$ mice have a shift in bacterial localization.

Dysbiosis of the small intestine is implicated in human diseases ranging from metabolic disorders (diabetes, obesity, malnutrition)[90, 91] to autoimmune disease (Crohn's disease[92-94], celiac disase[95]). Small intestine biofilm formation has been reported only in disease states[96-99], as noted in Poceviciute et al. 2023[87]. Additionally, in Crohn's disease, shifts in ileal 'mucosal-associated' bacteria have been linked to new onset disease[92], active disease versus remission[93], and inflamed versus uninflamed tissue within the same patient[94]. However, significantly less is known about how bacteria directly interact with the epithelial surface and maintain dysbiosis. Defects in microvilli organization have been implicated in Crohn's disease[6] and ulcerative colitis[36], but it remains unclear if the microvilli defects are causal or a consequence of prior damage, inflammation, or infection. Our data establishes that microvilli defects are sufficient to cause dysbiosis facilitating direct bacterial access to and colonization of the epithelial surface. Ultimately, the microbiome is comprised of both the microbiota and its host environment and morphology[100-102]. However, most microbiome studies take a microbe-centric approach using genetic sequencing to characterize population shifts in the microbiota without assessing changes in localization. A better understanding of the contribution of the host environment to dysbiosis is essential to effectively target dysbiosis with therapeutics. Given the loss of separation between luminal bacteria and the epithelium in the small intestine we observe in our study, investigation of bacteria localization should be considered when examining dysbiosis. The *Cdhr2*$^{\Delta epi}$ mouse model provides a platform to study bacterial communities at the epithelial surface to dissect environmental contributions to dysbiosis.

SFB are the most prominently visualized bacteria in the terminal ileum of *Cdhr2*$^{\Delta epi}$ mice. SFB are apathogenic, spore-forming bacteria that adhere to the epithelial surface via dense F-actin "holdfast points" and stimulate mucosal immunity[75, 103]. Typically, in the mouse model SFB colonize the terminal ileum shortly after weaning, then decline to low levels over several weeks[62, 63]. As expected, *Cdhr2*$^{fl/fl}$ mice have minimal SFB visualized by SEM or IF several weeks after weaning. In contrast, *Cdhr2*$^{\Delta epi}$ mice have persistently elevated levels of SFB colonizing the terminal ileum. The dense microvillar array of the brush border is a mechanical barrier that bacteria must bypass or disassemble to form actin-dependent attachments. IMAC tip links function to maintain the tightly packed microvillar array within each cell[4]. Loss of uniform microvillar organization and packing creates an opening that allows bacteria to attach to the epithelial surface. Early SFB attachments have not been characterized outside of electron microscopy 'snapshots' demonstrating possible microvilli distortion, elongation, or branching at sites of initial contact with the brush border. Initial contact is followed by invagination of the cell surface with the cell and SFB membranes closely apposed and surrounded by a dense accumulation of F-actin[69, 75, 104]. We observed initial SFB segments consistently co-localize with EPS8 and Arp2/3. The marked number of EPS8 positive adherent SFB most likely represent newly attached initial SFB segments from the intestinal lumen. Arp 2/3 is not present in brush border microvilli which contain parallel, bundled F-actin. SFB colocalization with Arp2/3 indicates remodeling of the apical cytoskeleton from bundled filaments into a branched network. Immature SFB filaments do not colocalize with Arp2/3 implying active remodeling is associated only with initial attachment. The pathogen, *Listeria monocytogenes*, uses Arp2/3 as an initial step to nucleate actin filaments, then augments filament elongation with the actin bunding protein Fascin[105]. Interestingly, multiple different actin bundling proteins were able to support this function *in vitro*[105]. Based on our data and the characterization of other bacteria life cycles, the actin bundler Espin could play a role in stabilizing and elongating actin filaments nucleated by Arp2/3. This is supported by our evidence that Espin is consistently present in both initial and mature SFB attachments (Figure 4D).

SFB are flagellated[106, 107], providing a means for intraluminal bacteria to reach the epithelial surface. While our data do not rule out the possibility that single adherent SFB are late-stage bacteria being shed from the epithelial surface, the high level of adherent single SFB in the *Cdhr2*$^{\Delta epi}$ ileum is consistent with autoinoculation from luminal reserves. SFB holdfast points contain a dense accumulation of F-actin[75], but additional molecular detail has not been elucidated. Electron microscopy demonstrates initial SFB segments are embedded in the host cell surface with bacteria and host membranes closely apposed but intact[104, 108]. Encircling the SFB holdfast, an electron dense layer (~35 nm thick)[104] lies within and immediately adjacent to the host membrane which is surrounded by a fine granular electron density[69, 104, 109, 110]. The granular electron density is consistent with the F-actin. Based on our data, EPS8 and ZO-1 are potential components of the electron dense plaque anchoring SFB.

One report noted that microvilli in contact with SFB were elongated and thinned, and branching of a microvillus was noted[111]. It is unclear which SFB lifecycle stage is captured in this representative image as it is high magnification and only a single

section. Mature microvilli are uniform in both diameter and length[10, 112], and branching is an unusual phenomenon. Branching has been characterized in immature, dynamic microvilli as a mechanism to generate new daughter microvilli[17]. EPS8 accumulates focally prior to microvillus branch formation[17]. Given our data demonstrating SFB holdfast segments recruit EPS8, this may represent an early step of SFB attachment with EPS8 stimulating microvilli elongation and branching. EPS8 is a component of the electron dense microvillus 'tip complex' and may contribute to the electron dense plaque in SFB holdfast attachments.

EPS8 is important for microvilli stability and has been implicated in actin bundling, capping, and nucleation dependent on its interactors[16, 17, 61]. Immature microvilli are dynamic, moving across the cell surface powered by treadmilling of the F-actin core[12] with loss of EPS8 resulting in rapid microvilli collapse and disassembly[17]. EPS8 also localizes to the tips of mature microvilli[60, 113] which have significantly slower actin turnover[114]. One possibility illuminated by the data in this manuscript is that EPS8 recruitment to nascent SFB attachments may competitively remove EPS8 from adjacent microvilli facilitating microvilli disassembly, further opening the brush border for bacterial attachment. This possibility is supported by others findings that EPS8 and Arp2/3 regulate the balance between linear and branched actin networks[115-117]. Additionally, bacterial pathogens utilize bacterial effector proteins to inhibit, displace, or competitively recruit EPS8 to modify the actin cytoskeleton[48, 118, 119]. EPEC and EHEC use distinct methods to displace EPS8 and 'hijack' cellular actin nucleation machinery to generate actin pedestals. Alternatively, *Chlamydia* recruits EPS8 to early inclusions mediating cell shape changes and transient loss of junctional integrity. EPS8 at early SFB attachments has multiple potential mechanisms to modify the surface actin.

SFB not only anchor preferentially at or near cell-cell junctions[63] but recruit ZO-1 to attachment sites. ZO-1 is a tight junction plaque protein[120] and a likely plaque protein in SFB holdfast attachments given its localization between the SFB and F-actin of the holdfast point. SFB may co-opt the tight junction machinery to trigger membrane invagination or to create a stable attachment[120, 121]. IMAC linkages not only maintain continuity of the microvilli within a single cell, but between adjacent cells (transcellular adhesion) ultimately generating a continuous microvillar array lining the intestinal surface[34]. Our data suggest that the transcellular IMAC linkages may function in part to mask cell-cell junctions from luminal bacteria with loss of this continuous array, thereby, increasing SFB access to the potentially vulnerable peri-junctional apical membrane for attachment.

SFB have been detected in organisms ranging from chickens to mice to primates[63, 122] with human-specific SFB reported in 2020[123, 124]. While SFB-like bacteria have been seen in humans with potential links to inflammatory processes[125, 126], the impact and extent of SFB colonization in humans remains unclear[127]. Genetic studies classify SFB as obligate/facultative symbionts[106, 128-131] with only one laboratory successfully culturing SFB *in vitro*[132]. Isolation and *in vitro* studies characterizing human SFB are hampered by their co-dependence on epithelial cells for *in vitro* growth and propagation[107, 132]. Studying SFB may improve the ability to culture other difficult to cultivate bacteria—

which are estimated to comprise up to 70% of the human gut microbiome[133]. Similar to SFB, these bacteria frequently have reduced genomes[134] and extensive spore formation to facilitate human to human transmision[135]. Our data provides multiple pathways for increased SFB access to the epithelial surface. As previously reported, SFB attach preferentially near cell-cell junctions[63], but our data revealed SFB filaments incorporate ZO-1 at their attachment sites in continuity with the cell-cell junctions. This is an exciting advancement in our understanding of the highly complex lifecycle of SFB. *In vitro* and live cell imaging studies would provide greater insight into the SFB lifecycle and co-dependence on the epithelium. Understanding SFB-host interactions in the ileum has multiple benefits. First, adherent bacteria are commonly pathogens but also pro-inflammatory bacteria that, like SFB, stimulate TH17 signaling and modify immune signaling[136]. While reported in humans, their direct role in human disease is unclear, but SFB can serve as a representative "adherent" bacterium as the gaps in host defense that allow persistent colonization may be exploited by other adherent bacteria. Second, insights into the complex lifecycle of organisms that require fastidious conditions or depend on host cells to complete normal physiologic and metabolic processes may help understand the difficult to grow bacteria that make up more than half of the human gut microbiome.

In summary the disruption of IMAC linkages between microvilli tips results in loss of the normal separation between luminal bacteria and the epithelial surface in the terminal ileum. Loss of this defensive barrier allows both actin-dependent adherent, and mucosal-associated bacteria to colonize the epithelial surface. While there is not a shift in the makeup of the microbiome, this altered localization represents dysbiosis. Utilization of a IMAC deficient model system could be used to understand commensals at the epithelial surface in a complex *in vivo* system.

STAR Methods

KEY RESOURCES TABLE

REAGENT or RESOURCE	SOURCE	IDENTIFIER
Antibodies		
Anti-Arp3 (ACTR3) (mouse) [1:100]	Santa Cruz	Cat# sc-48344
Anti-CD3 (rat), anti-mouse, PerCP/Cyanine5.5	BioLegend	Cat#100218
Anti-CD4 (rat), anti-mouse, Brilliant Violet 785	BioLegend	Cat# 100453
Anti-CD11b (rat), anti-mouse/human, PE/Cyanine5	BioLegend	Cat# 101210
Anti-CD45 (rat), anti-mouse, Alexa Fluor 700	BioLegend	Cat# 103128
Anti-CD45R/B220 (rat), anti-mouse/human, PerCP	BioLegend	Cat# 103234
Anti-CD8a (rat), anti-mouse, PE/Cyanine7	BioLegend	Cat# 100722
Aanti-EPS8 (mouse) [1:200 WM; 1:400 tissue sections]	BD Transduction Laboratories	Cat# 610144
Anti-ESPN (rabbit) [1:500]	Sigma-Aldrich	Cat# HPA028674
Anti-IL-17A (rat), anti-mouse, APC	BioLegend	Cat# 506916
Anti-INF-γ (rat), anti-mouse, Brilliant Violet 421	BioLegend	Cat# 505830
Anti-IRTKS (BAIAP2L1) (rabbit) [1:200]	Invitrogen	Cat# PA5-54365
Anti-Ly-6G (rat) anti-mouse, Brilliant Violet 510	BioLegend	Cat# 127633
Anti-TCR γ/δ (hamster), anti-mouse, APC/Cyanine7	BioLegend	Cat# 118144
Anti-Villin (rabbit) [1:50]	Santa Cruz	Cat# sc-28283
Goat anti-mouse Alexa Fluor 488 **F(ab')2** fragment [1:1000]	ThermoFisher	Cat# A-11017, RRID: AB_2534084
Goat anti-rabbit Alexa Fluor 568 F(ab')2 fragment [1:1000]	ThermoFisher	Cat# A-21069, RRID: AB_253573

Chemicals, peptides, and recombinant proteins		
Alexa Fluor 647 Phalloidin [1:200]	ThermoFisher/Invitrogen	Cat# A22287
DAPI (4',6-diamidino-2-pheylindole) [1:200 WM]	ThremoFisher	Cat# 62248
DMSO	Sigma	Cat# D8418
Ethyl Alcohol, Anhydrous (200 proof)	Decon Laboratories, Inc.	Cat# 64-17-5
Ethyl Alcohol, Anhydrous (200 proof)	Electron Microscopy Sciences	Cat# 15055
Glutaraldehyde, 25%	Electron Microscopy Sciences	Cat# 18220
HEPES Buffer	Sigma	Cat# P1851
Histo-Clear	National Diagnostics	Cat# HS-200
Hoechst 33342 [1:200 WM]	ThermoFisher	Cat# 62249
LIVE/DEAD (L/D) Fixable Violet Dead Cell Stain Kit	Invitrogen	Cat# L34955
Osmium Tetroxide	Electron Microscopy Sciences	Cat# 19112
Paraformaldehyde, 16%	Electron Microscopy Sciences	Cat# 15710
ProLong Gold Antifade Reagent	Invitrogen	Cat#P36930
Sucrose	Fisher Chemical	Cat# S5-3
Tannic Acid	Electron Microscopy Sciences	Cat# 21700
Triton X-100	Thermo Scientific	Cat# A16046.AP
Uranyl Acetate	Electron Microscopy Sciences	Cat# 22400

Experimental models: Organisms/strains		
CDHR2$^{fl/fl}$ mouse (CDHR2$^{fl/fl}$, villin-Cre$^{-/-}$)	Tyska Laboratory, Vanderbilt University	Pinette et al., 2019
CDHR2$^{\Delta epi}$ mouse (CDHR2$^{fl/fl}$, villin-Cre+$^{/-}$)	Tyska Laboratory, Vanderbilt University	Pinette et al., 2019
CDHR5 WT and KO mice	Gross Laboratory, INSERM UMR1260	Beck et al., 2021

Other		
Precision Cover Glasses, #1.5H Thickness, 012mm	ThermoFisher / THORLABS	Cat# NC1692862 / #CG15NH
Superfrost slides	ThermoFisher /	Cat # 12-550-15

Software and Algorithms		
FIJI	https://fiji.sc	N/A
FIJI Plugin, Z-stack Depth Color Code	https://github.com/UU-cellbiology/ZstackDepthColorCode	N/A
NIS AR Elements	Nikon	N/A
Imaris	Oxford Instruments	N/A
Prism 10	GraphPad	N/A
BioRender	Biorender	N/A

Mice

Animal experiments were carried out in accordance with American Veterinary Medical Association, Vanderbilt University Medical Center IACUC, and VA Medical Center Animal Care Guidelines, ACORP Animal Protocol Number V1900133. As previously described in Pinette et al.[35], Cdhr2$^{tm1c/tm1c}$ mice were crossed with villin-Cre$^{+/-}$;Cdhr2$^{tm1c/tm1c}$. The genotype in villin-expressing tissues becomes Cdhr2$^{tm1d/tm1d}$ which is non-expressing and referred to as Cdhr2$^{\Delta epi}$. Mice that do not express Cre retain the conditional allele, Cdhr2$^{tm1c/tm1c}$, express CDHR2, and are referred to as Cdhr2$^{fl/fl}$. Littermate Cdhr2$^{\Delta epi}$ and Cdhr2$^{fl/fl}$ mice were weaned and separated based on genotype (Supplemental Figure 1B), then mice were sacrificed per institutional guidelines at 5 to 8 weeks of age and ileum tissue was harvested. CDHR5 WT and KO mouse tissue was provided by Isabelle Gross, INSERM UMR_S1113, Université de Strasbourg, FMTS, Strasbourg, France.

Tissue Preparation

The distal most 3 cm of the mouse small intestine was dissected and flushed with 1.5 ml of ice-cold PBS. The unfixed, “washed” tissue was sub dissected and processed for multiple uses. After unfixed tissue was collected and snap frozen, the remaining tissue was immediately placed in fixative and further sub dissection completed in fixative as outlined below.

Microbiome Analysis

Biospecimens were collected at weaning (stool) and sack (stool and washed ileum tissue ~5 mm x 1 cm), snap frozen using liquid nitrogen or dry ice, then stored at -80˚C until further processing. Biospecimens were processed according to the PureLink Microbiome DNA Purification Kit (A29790) protocol from ThermoFisher. Purified DNA samples were submitted to the VANTAGE genomics core at Vanderbilt University for shotgun metagenomic sequencing. Quality Control analysis was performed on the DNA samples using a DNA Qubit assay. The samples were normalized, and libraries were prepared using the Twist Biosciences kit (P/N: 104207) following a miniaturized version of the manufacturers protocol. The library quality was assessed using the Agilent Bioanalyzer and quantified using a qPCR-based method with the KAPA Library Quantification Kit (P/N: KK4873) and the QuantStudio 12K instrument.

Prepared libraries were pooled in equimolar ratios, and the resulting pool was subjected to cluster generation using the NovaSeq 6000 System, following the manufacturer's protocols. 150 bp paired-end sequencing was performed on the NovaSeq 6000 platform targeting 10M reads per sample. Raw sequencing data (FASTQ files) obtained from the NovaSeq 6000 were subjected to quality control analysis, including read quality assessment. Real Time Analysis (RTA) Software and NovaSeq Control Software (NCS) (1.8.0; Illumina) were used for base calling. MultiQC (v1.7; Illumina) was used for data quality assessments.

Metagenomic analysis was conducted using the Illumina DRAGEN Metagenomics Pipeline (v3.5.12). The pipeline utilized the Kraken2 algorithm to carry taxonomic classification of reads, in conjunction with a MiniKraken2 (March 2020) taxonomic database. The pipeline incorporated the DRAGEN Map/Align and de-hosting function, enabling the removal of host genome sequences and the alignment of the sequence with the murine reference genome (mm10). A minimum alignment score of 50 was applied for de-hosting control. Taxonomic classification was executed by assigning taxonomic labels to DNA sequences based on k-mers within the query sequence against the reference database. The database maps k-mers to the lowest common ancestor (LCA) among all genomes. The taxa associated with k-mers, along with their ancestors, collectively formed the taxonomy tree for classification, while sequences lacking k-mers remained unclassified. Organism detection thresholds were set between 1 and 200. Krona plots, quality control (QC) metrics, and organism detection reports were generated.

The data was returned as Kraken files which were then uploaded to Galaxy[137] for further processing. The Bracken Abundance[138] was processed at the phylum level with a threshold of 5. The report was filtered to include only bacteria and used to create a

relative abundance graph in Prism (Figure 3H). The filtered phylum level Kraken report was loaded back into Galaxy. Krakentools[139] was used to calculate the alpha diversity (Simpson's Diversity Index and Berger Parker Dominance Index) and then graphed using Prism (Figure 3I). For the species analysis, the Bracken Abundance was processed at the species level with a threshold of 10. The report was filtered to include only include bacteria and species detected >2% were included in Figure 3J.

Whole Mount (WM) Tissue Immunofluorescence

The most terminal ~1 cm of the small intestine was excised (Cdhr2$^{fl/fl}$ and Cdhr2$^{\Delta epi}$ mice), flushed with ice cold PBS, and immediately placed in 2% PFA/PBS. Tissue was sub-dissected in fixative into small ~2 mm^3 pieces which were transferred to fresh 2% PFA/PBS and fixed for 1.5 h. Starting with fixation, samples were gently rocked for all incubation steps. Fixed tissue was washed three times with PBS, then permeabilized 30 m in 0.2% Triton/PBST (0.1% Tween 20 in PBS). Tissue was washed three times in PBST, and blocked in 5% normal goat serum (NGS)/PBST overnight at 4°C. Following block, tissue was washed three times with PBST and stained. Primary antibodies (listed below) were diluted in 1% NGS/PBS and incubated overnight at 4°C followed by three PBST washes. Secondary antibodies (listed below) were diluted in 1% NGS/PBS and incubated 4 h at RT in the dark, followed by three PBS washes. DAPI, Hoechst, and phalloidin were each diluted in 1% NGS or PBS and incubated 2 h at RT in the dark. Tissue was washed four times in PBS then mounted onto glass slides in ProLong Gold using acid-washed #1.5H precision coverslips (Thorlabs #CG15CH2) with the villus surface facing the glass coverslip. The following antibodies and dilutions were used for whole mount staining: anti-EPS8 (mouse BD Transduction Laboratories #610144), 1:400; anti-Villin (rabbit, Santa Cruz #sc-28283), 1:50; anti-ESPN (rabbit, Sigma-Aldrich #HPA028674), 1:500; anti-Arp3 (ACTR3) (mouse, Santa Cruz #sc-48344), 1:100; Goat anti-mouse Alexa Fluor 488 F(ab')2 fragment (Invitrogen #A-11017), 1:1000; Goat anti-rabbit Alexa Fluor 568 F(ab')2 fragment (Invitrogen #A-21069), 1:1000; Phalloidin 647 (Invitrogen #A22287), 1:200; and DAPI (ThermoFisher #62248), 1:200; and Hoechst 33342 (ThermoFisher #62249), 1:200. Secondary antibodies (not including phalloidin, DAPI, or Hoechst) were centrifuged at 4˚C for 10 m at a speed of 21,000 x g prior to use.

Frozen Section Tissue Preparation

Tissue was placed in 2% PFA and further sub dissected in fixative into pieces ~2mm^2, then fixed for an additional 30 minutes at RT, total fixation time ~60 minutes. After fixation, the tissue samples were washed three times with PBS. Samples were placed in 30% sucrose villi-side down and incubated overnight at 4°C. Then samples were then washed in optimal cutting temperature (OCT) compound by passing the tissue through 3 separate blocks of OCT. Samples were oriented will villi pointing laterally, perpendicular to the lab bench, in a fresh block of OCT and snap frozen in dry ice-cooled ethanol. Using cryostat Leica CM2050-S samples were cut into 10µm thin sections and mounted on Superfrost Plus Microscope Slides (fisherbrand) and stored at -20°C until staining.

Frozen Section Immunofluorescence

Slides were thawed to RT and washed twice with PBS. Samples were permeabilized using 0.2% Triton X-100 in PBS for 30 minutes at RT. Coverslips were washed with PBS, blocked in 5% normal goat serum (NGS) in PBS overnight at 4˚C in a humidified chamber. Following block, tissue was washed three times with PBS. Primary antibodies (listed below) were diluted in 1% NGS/PBS and incubated on the samples overnight at 4°C in a humidified chamber followed by three PBS washes. Secondary antibodies (listed below) were diluted in 1% NGS/PBS and incubated 4 h at RT in a dark humidified chamber, followed by three PBS washes. DAPI, Hoechst, and phalloidin were each diluted in 1% NGS or PBS and incubated 2 h at RT in the dark. Finally, samples were washed 4 times with PBS and mounted in ProLong Gold using acid-washed #1.5H precision coverslips (Thorlabs #CG15CH2). Samples were left in a dark chamber at RT overnight to cure. The following antibodies/stains and dilutions were used: Anti-EPS8 (mouse, BD Transduction Laboratories Cat# 610144), 1:200; Anti-E-cadherin (mouse, BD Transduction Laboratories Cat# 610182), 1:100; Anti-ZO-1 (rabbit, Invitrogen #61-7300), 1:50; goat anti-mouse Alexa Fluor 488 F(ab')2 fragment (Invitrogen Cat# A-11017), 1:1000; goat anti-rabbit Alexa Fluor 568 IgG (H+L) (Invitrogen Cat# A-11011), 1:500; Alexa Fluor 647 Phallodin (Invitrogen Cat# A22287), 1:200. Secondary antibodies were centrifuged at 4˚C for 10 m at a speed of 21,000 x g prior to use. Samples mounted in ProLong Gold and allowed to cure before imaging.

Paraffin Section Tissue Preparation

After washing with ice cold PBS, mouse ileum was placed in 2% PFA and further sub dissected into pieces ~2 mm^2. After a total of 2 hours in fixative, samples were placed in a tissue cassette, transferred to 70% EtOH and submitted to the Vanderbilt University Translational Pathology Shared Resource to be embedded in paraffin wax. Using a Microm HM-325 microtome samples were cut into 7-15 µm sections and mounted on glass slides and stored at RT until staining.

Paraffin Section Immunofluorescence

Paraffin slides were de-paraffinized by placing on a 60˚C slide warmer followed by two Histoclear washes. Slides were rehydrated through an ethanol gradient (EtOH 100% x2, 95% x2, 70%), then 20 mM Tris-HCl, pH8. After rehydration, samples were processed as above for Frozen Section Immunofluorescence.

Fluorescent *in situ* Hybridization (FISH)

Samples were hybridized with FISH probes after permeabilization/blocking but before primary and secondary antibody staining as follows. Samples were incubated with FISH probe SFB1008-CY3 (5'-Cy3-GCGAGCTTCCCTCATTACAAGG-3', Sigma Genosys Custom Oligo)[65, 66] at 2 µM in Hybridization Buffer (20 mM Tris-HCl pH 8.0, 0.9 M NaCl, 0.01% SDS) in a dark, humidified, hybridization chamber for 2 hours at 46°C. Samples were then washed in FISH Wash Buffer (20 mM Tris-HCl pH 8.0, 225 mM NaCl, 5 mM EDTA). Following wash step, samples were incubated with antibody or other stains as out lined above. FISH probes were centrifuged at 4˚C for 10 m at a speed of 21,000 x g prior to use.

Electron Microscopy

Steps are completed at room temperature (RT) unless indicated otherwise. Following wash with PBS (phosphate buffered saline), tissue is placed in 4% paraformaldehyde (PFA)/PBS and sub-dissected into small pieces ~5 mm or less using a stereo dissecting microscope, then transferred to a large volume (5-10 mL) of EM fixative (2.5% glutaraldehyde, 4% PFA in SEM Buffer to complete fixation 1 h. SEM Buffer consisted of either PBS or 0.1M HEPES, pH 7.3 with subsequent washes in the corresponding Buffer (without Ca). Samples were washed 3x in SEM Buffer, then incubated in 1% tannic acid/SEM Buffer for 1 h. Tissue was washed 3x with ddH_2O followed by 1 h incubation with 1% osmium tetroxide/ddH_2O. Tissue was washed three times with ddH_2O, then incubated 30 m with 1% uranyl acetate/ddH_2O. Samples were washed three times in ddH_2O, then dehydrated in a graded ethanol series and dried using critical point drying (*Cdhr2*$^{fl/fl}$ and *Cdhr2*$^{\Delta epi}$ mouse tissue samples) or chemically with hexamethyldisilazane (*Cdhr5* WT and *Cdhr5* KO mouse tissue samples). Samples were mounted on aluminum stubs and sputter coated with platinum (*Cdhr2*$^{fl/fl}$ and *Cdhr2*$^{\Delta epi}$ samples) or gold/palladium (*Cdhr5* WT and *Cdhr5* KO tissue samples) using a Cressington 108 sputter coater. Imaging was performed using a Quanta 250 Environmental SEM operating in high-vacuum mode with an accelerating voltage of 5-10 kV (Figure 1B-E, 5A) or Zeiss Crossbeam 550 operated at 2 kV using the lower secondary electron detector (Figure 4G, 5B).

Whole Mount Fluorescence Microscopy

Laser scanning confocal microscopy was performed on a Nikon FN1 upright light microscope equipped with an A1 R HD25 laser-scanning head, four excitation lasers (405, 488, 561, and 640 nm), and a 60x/1.4 NA objective. All images used for quantitative comparisons were prepared with equal treatment, acquired with identical parameters (e.g. pinhole diameter and detector gain), and processed in an identical manner.

Fluorescence Microscopy

Laser scanning confocal microscopy of whole mount samples was performed on a Nikon FN1 upright light microscope equipped with an A1 R HD25 laser-scanning head, four excitation LASERs (405, 488, 561, and 647 nm), and a 60x/1.4 NA objective. All images used for quantitative comparisons were prepared with equal treatment, acquired with identical parameters (e.g. pinhole diameter and detector gain), and processed in an identical manner. Spinning disk confocal microscopy of tissue sections was performed using a Nikon Ti2 inverted light microscope with a Yokogawa CSU-W1 spinning disk head with SoRA, a Hamamatsu Fusion BT sCMOS camera, and four excitation LASERs (405, 488, 568, and 647 nm). A 60x/1.49 NA TIRF oil immersion or 100x/1.45 NA oil immersion objective was used. To visualize protein localization at individual bacteria attachment sites, we performed confocal imaging with oversampling followed by deconvolution.

Image Processing

Images were contrast-enhanced and cropped using a combination of ImageJ/FIJI software from the National Institutes of Health (NIH), Nikon Elements, and Imaris. Post-processing to segment DAPI images into cellular nuclei and bacterial DNA was

completed using either (a) Labkit pixel classification[140] with FIJI, (b) Labkit pixel classification with FIJI plus Imaris or (c) Imaris built-in machine learning segmentation. Deconvolution was completed using Nikon Elements. Image stacks were viewed as single confocal planes, three-dimensional renderings (Nikon Elements or Imaris), or as a maximum intensity projection (maxIP) generated in ImageJ/FIJI, Nikon Elements, or Imaris. Dual-depth-coded images were generated as separate images in ImageJ/FIJI using the "Z-stack Depth Color Code" plugin then combined into a single image as a MaxIP.

RNA Isolation and Real Time qRT-PCR

RNA was isolated from washed ileum tissue from paired sets of *Cdhr2*$^{fl/f}$ and *Cdhr2*$^{\Delta epi}$ littermates at 5 to 8 weeks of age using TRIzol (Invitrogen) as described by the manufacturer followed by an RNA clean up protocol using the Qiagen RNAeasy kit. RNA was transcribed to cDNA using Thermo Fisher Scientific HighCapacity cDNA Reverse Transcription Kit (ThermoFisher Scientific, Waltham, MA, USA) per the manufacturer's specifications and then Taqman based real time rtPCR was performed using TaqMan Fast Advanced Master Mix (ThermoFisher Scientific, Waltham, MA, USA) and Taqman gene expression assays on the Applied Biosystems QuantStudio 6 Flex instrument. Relative Units were quantified using the relative gene expression. In short, all samples were calibrated to a pooled control sample prepared from control mice. Relative units were calculated using the $2^{\wedge -\Delta\Delta Ct}$ method, where the ΔCt is calculated as the difference in the cycle threshold of the gene of interest from the endogenous control gene (*Gapdh*) and then the ΔΔCt is the difference between the ΔCt of the sample compared to the control sample. Primer and probe sets were purchased as Taqman Gene Expression Assays from Applied Biosystems [mouse primer sets: *Cxcl1* Mm04207460_m1, *Il22* Mm01226722_g1, *Il6* Mm00446190_m1, *Il17a* Mm00439618_m1, *Reg3g* Mm00441127_m1 and *Gapdh* Mm99999915_g1].

<u>Method for Flow Cytometry:</u>

Single-cell suspensions were prepared from mouse spleens and lymph nodes by mechanical dissociation through 40 µm strainers into T cell media, followed by RBC lysis (1 mL RBC lysis buffer, 1 min, quenched with 20 mL PBS + EDTA) and centrifugation (350 × g, 7 min, 4 °C). Cells were stained with Fixable Violet Dead Cell Stain (Invitrogen, #L34955) diluted 1:1000 in PBS for 30 min at 4 °C in the dark, washed, and surface-stained in 100 µL MACS buffer for 30 min at 4 °C with CD45-AF700 (BioLegend #103128), CD3-PerCP-Cy5.5 (#100218), CD4-BV785 (#100453), CD8-PE-Cy7 (#100722), γδT-APC-Cy7 (#118144), B220-PerCP (#103234), Ly6G-BV510 (#127633), and CD11b-PE-Cy5 (#101210). Cells were fixed with Reagent A (Fix & Perm Kit, Thermo Fisher, Cat# GAS003) for 20 min at RT, washed, and permeabilized in Reagent B containing IL-17A-APC (#506916) and IFNγ-BV421 (#505830) for 30 min at RT in the dark. Fluorescence minus one (FMO) controls contained all antibodies except the omitted parameter, and single-color compensation controls were prepared with antibody capture beads. Data were acquired on a Cytek Aurora flow cytometer and analyzed using standard gating strategies.

QUANTIFICATION AND STATISTICAL ANALYSIS

Ratio of bacterial F-actin attachments to cell nuclei quantification

Using ImageJ/FIJI, the standard depth in Z analyzed was 50-150μm to account for the variable angles and positions of villi in a sample. Villi positioned at an angle were analyzed in increments down the Z plane to keep the consistent depth of 50-150μm. DAPI signal was used to quantify the number of nuclei within the selected depth. F-actin attachments perpendicular to the Z plane were identified by visualization of a circular ring that constricted to a point as the Z plane moved from surface to within the villus. Horizontal F-actin attachments were identified by visualization of triangular inclusions along the villus edge when parallel to the Z plane. To accurately visualize F-actin attachments throughout the selected depth the brightness and contrast of the image were adjusted for each plane. The sums of both the nuclei and F-actin attachments were used to calculate the ratio. The same approach was taken quantify the F-actin attachments positive for EPS8.

Bacteria DNA Pattern Quantification

To quantify the bacteria DNA patterns observed in sectioned tissue, the previously quantified sums of bacteria documented in Figure 2G/H were used as the total bacteria in a sample. Then images were evaluated across multiple z-steps to determine if bacteria were single, filamentous or indeterminate (most commonly due to high concentrations of bacteria). Quantification was blinded for the source of tissue (*Cdhr2*$^{fl/fl}$ or *Cdhr2*$^{\Delta epi}$).

Distance from Cell Junction Quantification

Confocal images were opened in ImageJ/FIJI and the measuring tool was used to record the distance from the center of the bacteria to the closest visible cell junction.

Analysis of Signal Intensity at Bacterial Attachment Sites

To measure signal intensities at bacterial attachment sites, 1-pixel wide line scans were drawn either transverse parallel to the cell surface or longitudinal from intracellular through the attachment site to extracellular. All intensity values were normalized (range set from 0 to 1). The intensity was normalized for each channel and fit to a Gaussian curve or a sum of 2 Lorentzian curves using PRISM v. 10.6.1 (GraphPad).

Statistical Analysis

Statistical significance was performed using the Mann-Whitney test (Figure 2G-H, Figure 5C), Friedman test (Figure 3I), unpaired T test (Supplemental Figure 1C), and paired Wilcoxon test (Supplemental Figure 1F-G). All statistical analysis was computed in PRISM v. 10.6.1 (GraphPad).

Figures and Figure Legends

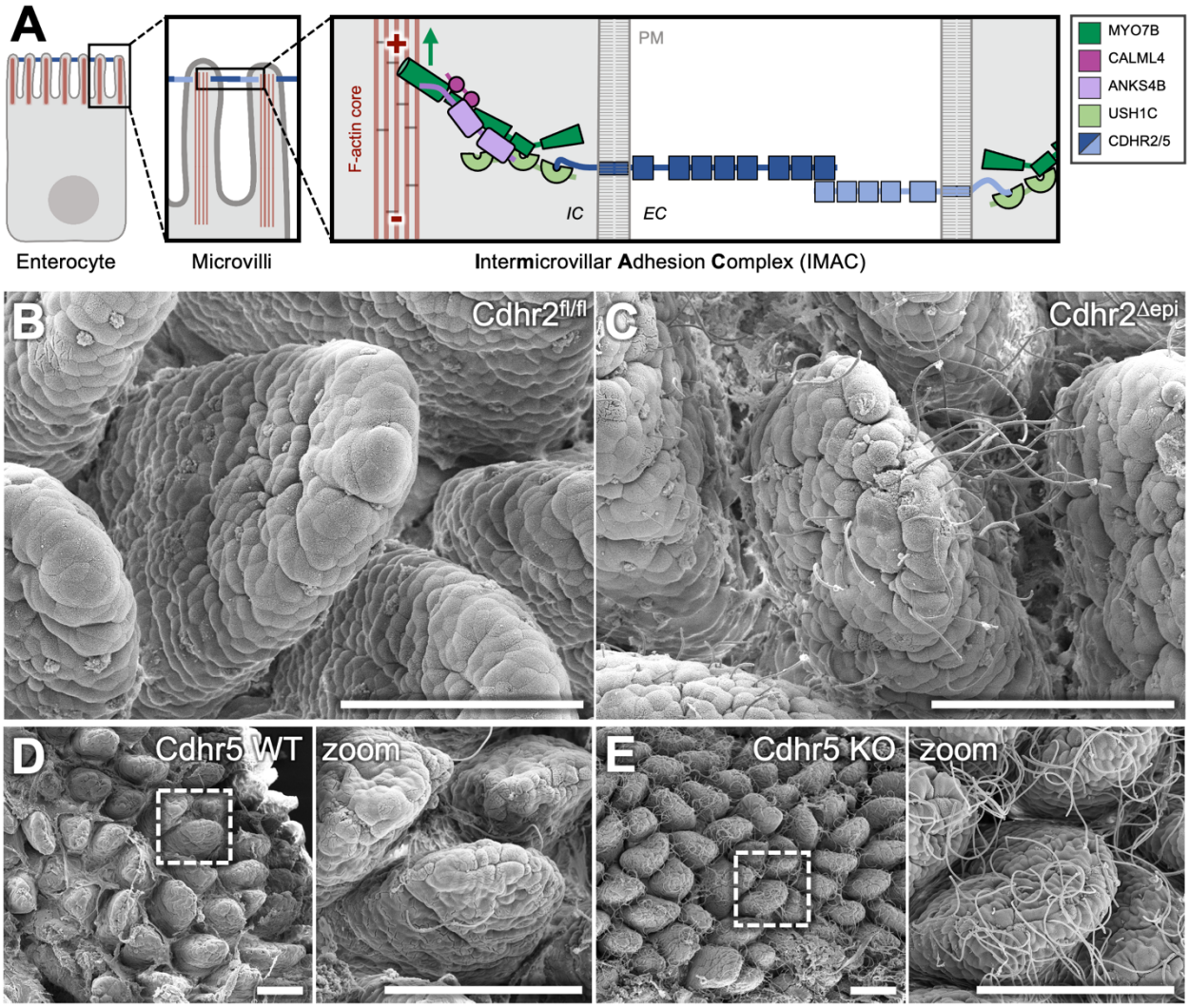

Figure 1. Mice with a disrupted IMAC have increased adherent bacteria in the terminal ileum. (A) Diagram highlighting components of the intermicrovillar adhesion complex (IMAC) at the tips of microvilli. PM = plasma membrane, IC = intracellular, EC = extracellular. Red "+" and "-" indicate F-actin barbed and pointed ends, respectively. Green arrow indicates F-actin barbed-end directed motion of MYO7B. (B) Representative SEM image of Cdhr2$^{fl/fl}$ mouse terminal ileum. (C) Representative SEM image of Cdhr2$^{\Delta epi}$ mouse terminal ileum. (D) Representative SEM image of Cdhr5 WT mouse terminal ileum. Boxed area enlarged in zoom. (E) Representative SEM image of Cdhr5 KO mouse terminal ileum. Boxed area enlarged in zoom. Scale bars 100 μm (B-E).

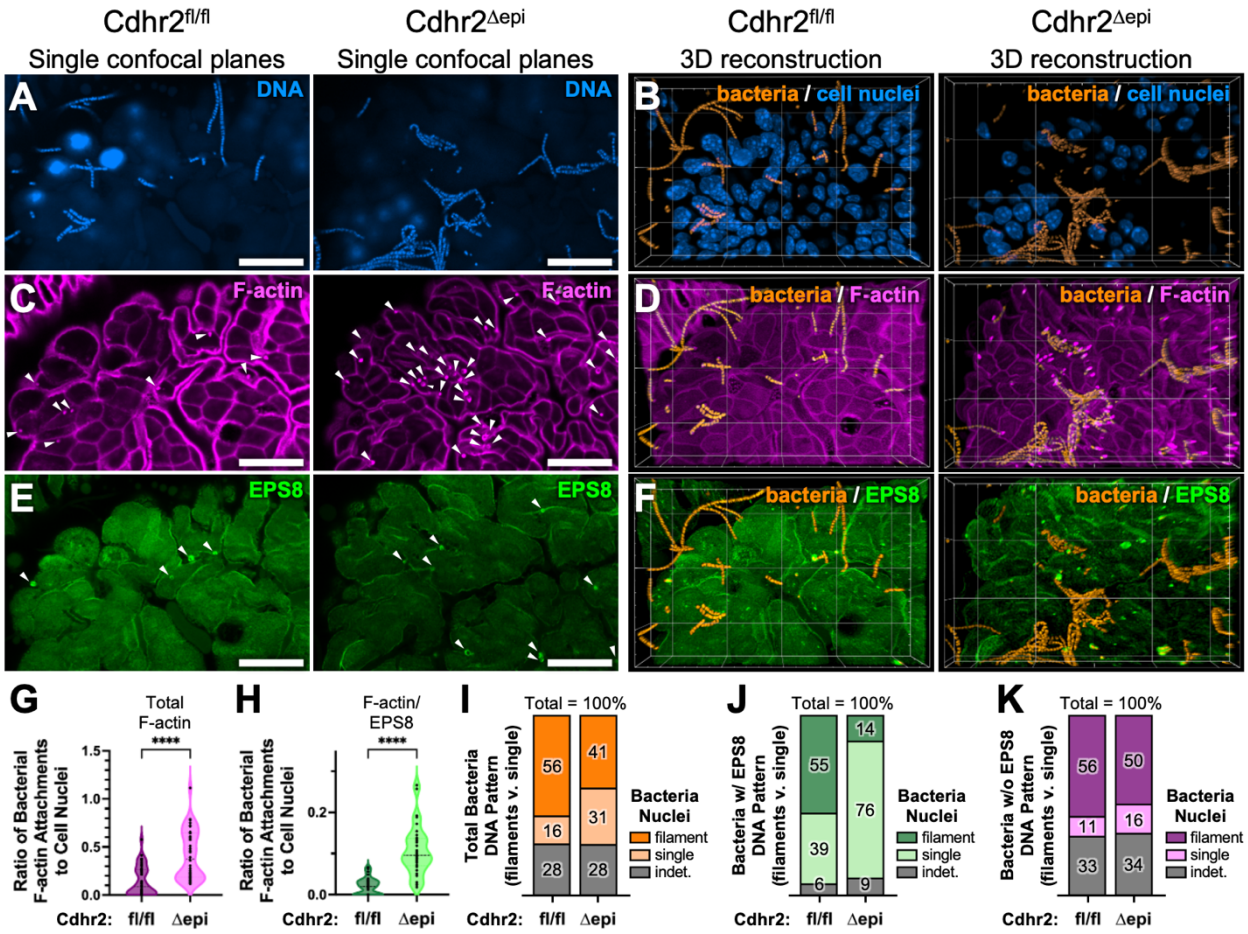

Figure 2. Mice with disrupted intermicrovillar adhesion have multiple populations of adherent bacteria enriched in the terminal ileum. Whole mount confocal images of ileum tissue comparing Cdhr2$^{fl/fl}$ and Cdhr2$^{\Delta epi}$ littermates. (A) Single confocal plane stained with DAPI to mark DNA. (B) 3D rendering of DAPI segmented using an artificial intelligence (AI) algorithm to isolate and differentially contrast bacterial DNA (orange) compared to cell nuclei (blue). (C) Single confocal plane stained with phalloidin to mark F-actin (actin-dependent adherent bacteria, white arrowheads). (D) 3D rendering of AI segmented bacterial DNA (bacteria) and phalloidin (F-actin). (E) Single confocal plane stained for EPS8 (actin-dependent adherent bacteria with EPS8, white arrowheads). (F) 3D rendering of AI segmented bacterial DNA (bacteria) and EPS8. (G-H) Quantification of actin-dependent adherent bacteria (Total F-actin, G) or actin-dependent adherent bacteria with EPS8 (F-actin/EPS8, H) relative to epithelial cell nuclei on distal villi. Each data point represents counts from one villus. For G, n = 39 Cdhr2$^{fl/fl}$ villi (765 bacterial attachments / 5921 cell nuclei) and n = 40 Cdhr2$^{\Delta epi}$ villi (2389 attachments / 5657 cell nuclei) taken from 5 sets of paired littermates. For H, n = 33 Cdhr2$^{fl/fl}$ villi (95 bacterial attachments / 5134 cell nuclei) and n = 33 Cdhr2$^{\Delta epi}$ villi (456 attachments / 4469 cell nuclei) taken from 4 sets of paired littermates. Violin plots with a dotted line at the median. Significance calculated using the Mann-Whitney test, **** $p < 0.0001$. Median 0.085 v. 0.377 actin-dependent bacterial attachments/epithelial cell in Cdhr2$^{fl/fl}$ and

Cdhr2$^{\Delta epi}$ villi respectively. Median 0.022 v. 0.096 actin-dependent bacterial attachments with EPS8/epithelial cell in Cdhr2$^{fl/fl}$ and Cdhr2$^{\Delta epi}$ villi respectively. (I-K) Stacked bar charts of adherent bacteria utilizing F-actin attachments by bacterial DNA morphology (filament, single, or indeterminate) total F-actin adherent bacteria (I) total F-actin adherent bacteria with EPS8 (J) and F-actin adherent bacteria without EPS8 (K). Scale bars 20 μm (A,C,E), and background grid 20 μm (B,D,F).

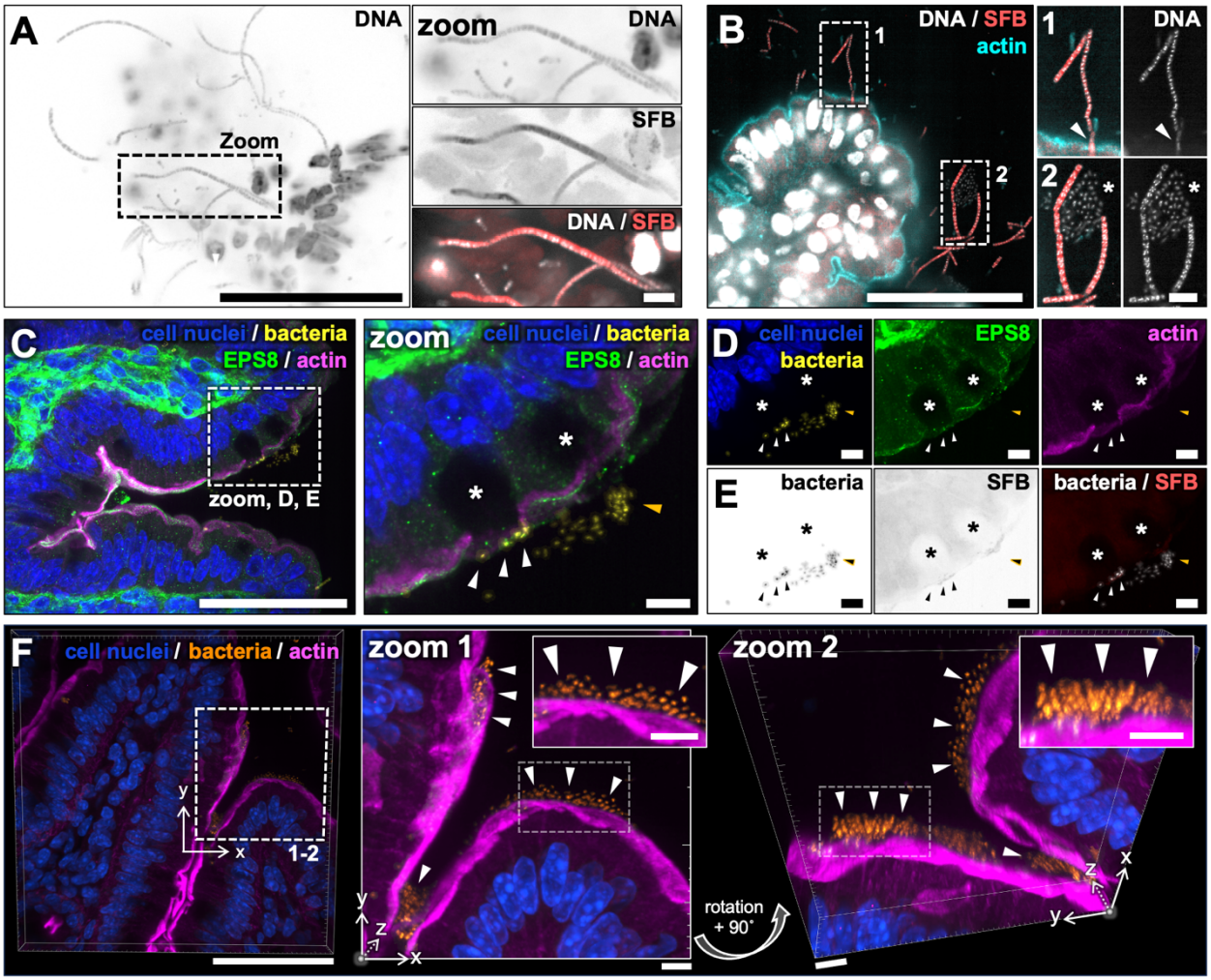

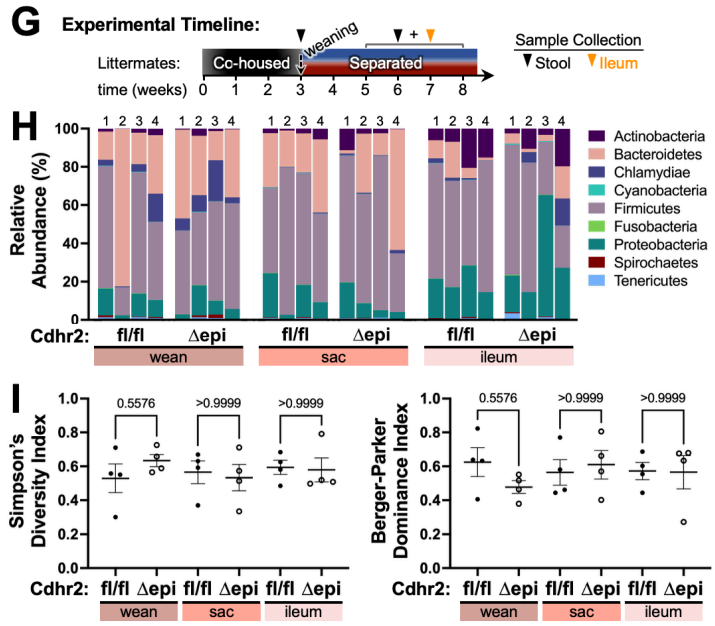

J

Phyla	Species	Cdhr2: fl/fl				Δepi				Func.
		Relative Abundance (%)								
Actinobacteria	Curtobacterium flaccumfaciens	6	6	25	15	---	10	---	23	PL
	Streptomyces lividans	---	---	3	---	---	---	---	3	ENV
Bacteroidetes	Bacteroides caecimuris	---	8	---	---	---	---	---	11	PI
	Bacteroides vulgatus	---	4	---	---	---	---	---	5	M
Chlamydiae	Chlamydia muridarum	3	---	---	---	---	6	---	21	OP
Firmicutes	Blautia producta	---	44	---	---	---	---	---	---	C
	Candidatus Arthromitus sp.*	59	---	---	70	---	61	8	---	C
	Lachnoclostridium sp. YL32	---	11	3	---	---	---	---	---	CA
	Lactobacillus johnsonii	---	---	4	---	5	---	4	---	C
	Lactobacillus murinus	3	3	37	---	50	6	12	8	C
	Lactobacillus reuteri	---	---	7	---	4	---	3	---	C
	Staphylococcus aureus	---	---	---	7	---	---	---	---	PATH
	Staphylococcus cohnii	3	---	---	---	---	---	---	---	C
	Staphylococcus xylosus	---	---	---	---	---	5	---	---	C
Proteobacteria	Bradyrhizobium sp. SK17	---	---	---	---	---	---	8	---	PL
	Helicobacter hepaticus	---	6	---	---	---	---	---	4	PATH
	Helicobacter typhlonius	9	---	4	---	6	---	4	3	OP
	Klebsiella oxytoca	---	5	13	6	---	7	---	16	OP
	Mesorhizobium soli	---	---	---	---	3	---	29	---	PL
	Pseudomonas tolaasii	---	---	---	---	---	---	3	2	F
	Ralstonia insidiosa	---	---	---	---	---	---	5	---	OP
	Variovorax paradoxus	---	---	---	---	---	---	5	---	PL
	Variovorax sp. PMC12	---	---	---	---	---	---	5	---	PL
	Xanthomonas euvesicatoria	13	---	---	---	---	---	---	---	PL

Notes: "---" < 2%, C: commensal, CA: cancer-associated, ENV: environmental, F: fungal bacteria, M: mutualist, OP: opportunistic pathogen, PATH: pathogen, PI: pro-inflammatory, PL: plant bacteria, *SFB-mouse and SFB-mouse-NL.

Figure 3. Loss of intermicrovillar adhesion facilitates polymicrobial tissue colonization with bacteria utilizing actin-dependent and actin-independent surface attachments. (A) Single confocal slice of Cdhr2$^{\Delta epi}$ ileum frozen section stained for DNA (Hoechst) and SFB 16S-rRNA fluorescence *in situ* hybridization (SFB FISH). Boxed area enlarged in zoom. (B) Deconvolved single confocal slice of paraffin sectioned Cdhr2$^{\Delta epi}$ mouse ileum stained for DNA (DAPI), SFB 16S-rRNA FISH (SFB), and actin. Boxed areas enlarged in Zooms 1 and 2 contrast adjusted to visualize bacteria. (Zoom 1-2) left images show a 3-color overlay DNA (white), SFB (red), actin (cyan), and right images with DNA only. White arrowhead highlights bacteria interaction with the surface actin/brush border, and the asterisk marks a cluster of bacteria negative for SFB 16S-rRNA FISH. (C) Maximum intensity projection (maxIP, depth 11.25 µm) of paraffin sectioned Cdhr2$^{\Delta epi}$ mouse ileum stained for DNA (DAPI), EPS8, and actin. DAPI segmented using an AI algorithm to isolate and differentially contrast bacteria (yellow) relative to cell nuclei (blue). Boxed area enlarged in Zoom, D, and E. Asterisks mark goblet cells, arrowheads highlight bacteria associated with goblet cells/mucus. (D) Individual channels from C, segmented DAPI (cell nuclei/bacteria), EPS8, and actin. (E) Individual channels from C inverted and shown in grayscale, segmented DAPI (bacteria), SFB 16S-rRNA FISH (SFB), and overlay. (F) 3D rendered maxIP (depth 8.40 µm) of paraffin sectioned Cdhr2$^{\Delta epi}$ ileum stained for DNA (DAPI) and actin. DAPI is AI segmented to isolate and differentially contrast bacteria (orange) relative to cell nuclei (blue). Boxed areas—enlarged and contrast enhanced (zoom 1); enlarged, contrast enhanced and rotated (zoom 2)—to visualize tissue-associated bacteria. Boxed areas in zoom images further enlarged and contrasted in insets, upper right. White arrowheads indicate bacteria. (G) Diagram of the experimental timeline. Paired Cdhr2$^{fl/fl}$ and Cdhr2$^{\Delta epi}$ littermates are co-housed until weaning. Stool collected at weaning (~3 weeks of age), then mice are housed separately by genotype. Stool and ileum tissue are collected between 5-8 weeks of age. (H) Relative abundance of bacterial phyla shown as stacked bar graphs. Samples collected from Cdhr2$^{fl/fl}$ and Cdhr2$^{\Delta epi}$ mice (sets 1-4); Stool at Wean (Wean), Stool at sacrifice (Sac), ileum tissue at sacrifice (Ileum). (I) Bacteria phylum alpha diversity. Simpson's Diversity Index (left) and Berger-Parker Dominance Index (right). Error bars represent mean ± SEM. Significance calculated using the Friedman test. (J) Table of bacteria species relative abundance detected > 2%. Scale bars: 50 µm (A), 5 µm (A, zoom), 50 µm (B), 5 µm (B, zoom 1-2), 50 µm (C), 5 µm (C, zoom), 5 µm (D), 5 µm (E), 50 µm (F), 5 µm (F, zooms 1-2 and insets).

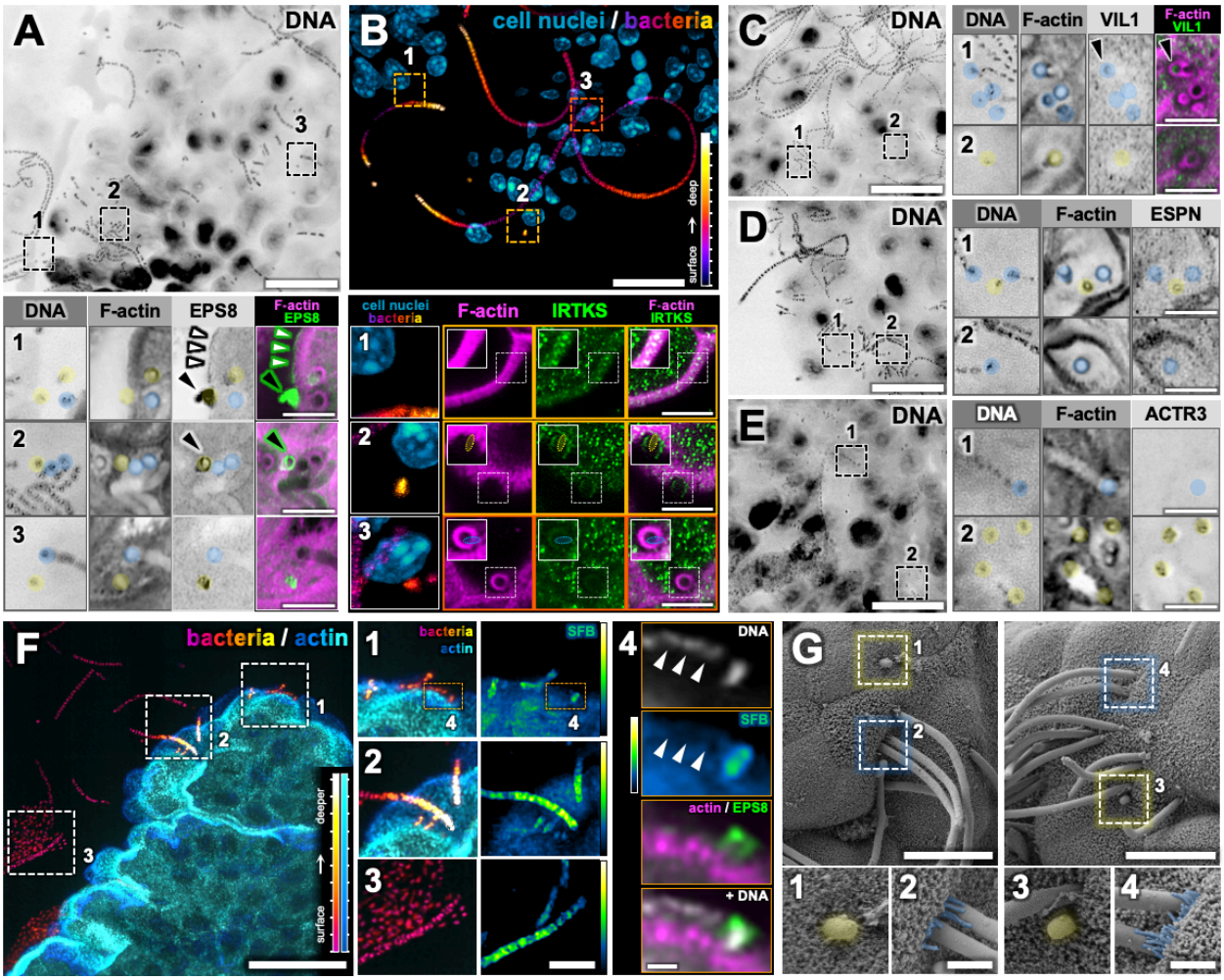

Figure 4. Adherent primary SFB segments recruit microvilli tip proteins (EPS8 and IRTKS) and remodel the actin cytoskeleton via Arp2/3. (A) Single confocal plane at the villus surface of Cdhr2$^{\Delta epi}$ mouse ileum whole mount tissue stained with DAPI (DNA). Boxed areas enlarged (zooms 1-3) with additional stains DAPI (DNA), phalloidin (F-actin), EPS8, and F-actin/EPS8 overlay. Adherent bacteria marked with a transparent overlay (yellow, single bacteria; blue, filaments). White arrowheads highlight EPS8 localization in enterocytes (zoom 1). Teardrop-shaped bacteria indicated by black arrowheads (zooms 1-2). (B) Cdhr2$^{\Delta epi}$ mouse ileum frozen tissue section stained with DAPI (DNA), deconvolved, AI segmented to isolate and differentially contrast bacterial DNA and viewed as a maxIP (depth 12.6 µm). The bacteria channel is z-depth color-coded; closer bacteria purple/magenta, deeper bacteria yellow/white, z-depth color-code at right. DNA from cell nuclei (cyan/blue). Boxed areas enlarged below (zooms 1-3) with the box color indicating the z-depth of the zoom images. (B, zoom 1) IRTKS localization in the enterocyte brush border. (B, zooms 2-3) highlights adherent bacteria. Column 1 is the main image panel enlarged (maxIP, depth 12.6 µm). Subsequent columns 2-4 show additional stains phalloidin (F-actin), IRTKS, and F-actin/IRTKS overlay as a maxIP (depth 0.3 µm). White boxed areas within zoom images (columns 2-4) are contrast enhanced and shown as insets (upper left) with bacteria localization

indicated by ovals (yellow, single bacteria; blue, filaments). (C-E) Single confocal planes at the villus surface of Cdhr2$^{\Delta epi}$ mouse ileum whole mount tissue stained with DAPI (DNA). Boxed areas (zooms 1-2) enlarged at right. DAPI (DNA) and phalloidin (F-actin) are shown in all sets plus Villin (VIL1, C), F-actin/VIL1 (C), Espin (ESPN, D), and Arp3 (ACRT3, E). (C, zoom 1), black arrowheads indicate a filamentous attachment with eccentric VIL1 localization. (F) Cdhr2$^{\Delta epi}$ mouse ileum paraffin tissue section stained for DAPI (DNA) and actin, deconvolved, and viewed as a maxIP (depth 10.4 μm). A z-depth color-code is applied to each channel, scales lower right. DNA AI segmented to isolate bacteria, cell nuclei are not displayed. Boxed areas enlarged at right (zooms 1-3). Column 1, bacteria/actin maxIP (depth 10.4 μm) enlarged from the main panel. Column 2, intensity color-coded SFB FISH (SFB) maxIP (depth 10.4 μm), intensity scale at right). Boxed areas in zoom 1 further enlarged in zoom 4. Z-depth indicated by box color, based on the main panel bacteria z-depth color-code. (F, zoom 4) Single confocal plane of surface bacteria with additional stains; DAPI (DNA) without AI segmentation, SFB FISH (SFB) intensity color-coded, actin/EPS8 overlay, and actin/EPS8 plus DNA overlay. White arrowheads indicate SFB FISH negative bacteria. (G) SEM images of Cdhr2$^{\Delta epi}$ mouse terminal ileum. Boxed areas enlarged in zooms 1-4 to highlight adherent bacteria (yellow, single bacteria; blue, filaments). (G, zooms 1, 3) single bacteria. (G, zooms 2, 4), filamentous bacteria with elongated microvilli at the base. Scale bars: 20 μm (A-F, main panels), (B, F) z-depth color-code tick marks at 1 μm intervals, 5 μm (A-F zooms 1-3), 2.9 μm (B, zoom 1-3, insets), 1 μm (F, zoom 4), 10 μm (G, main panel), 2 μm (G, zooms 1-4).

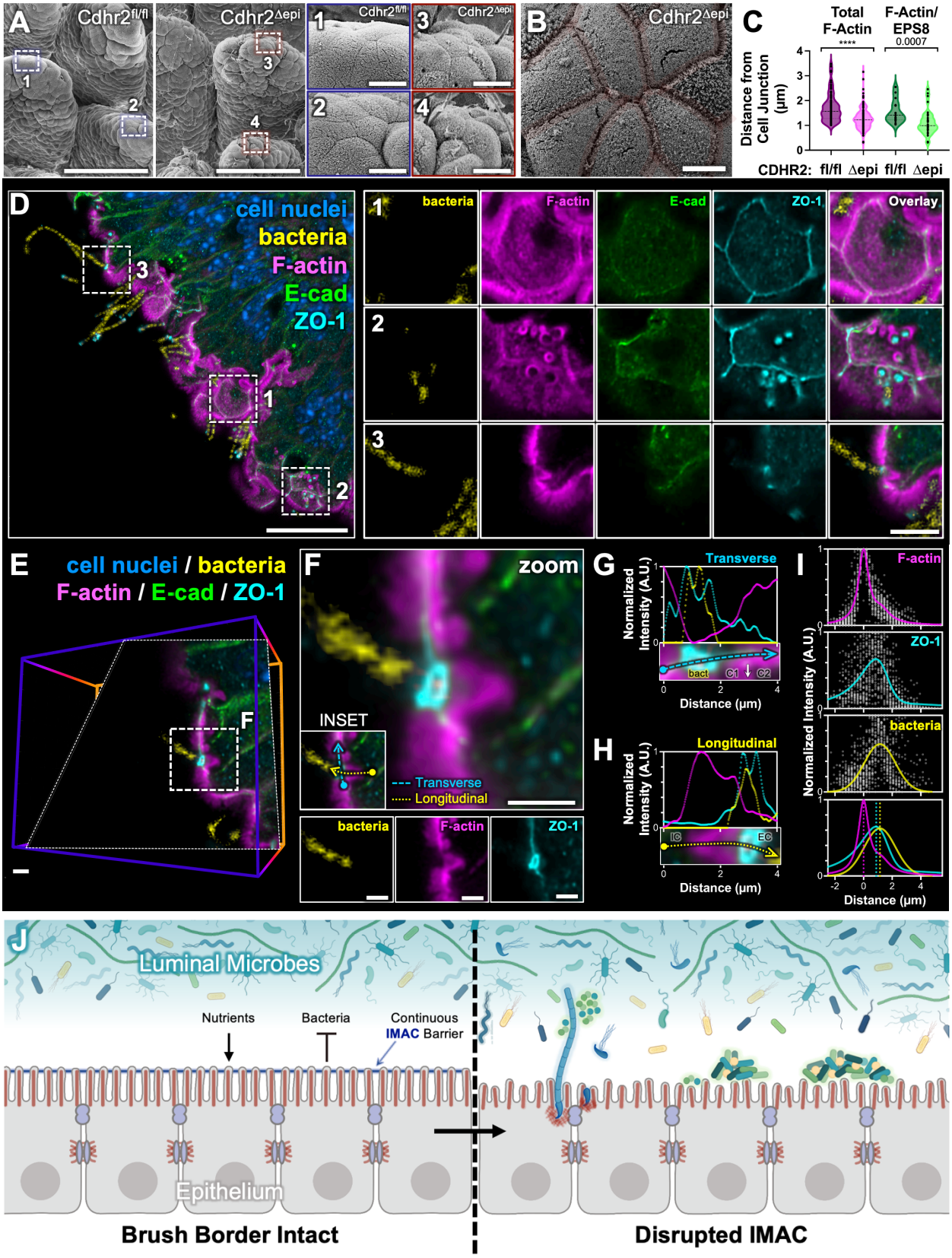
A
Cdhr2fl/fl
Cdhr2Δepi
B
Cdhr2Δepi
C
Total F-Actin
F-Actin/ EPS8
****
0.0007
Distance from Cell Junction (µm)
CDHR2: fl/fl Δepi fl/fl Δepi
D
cell nuclei
bacteria
F-actin
E-cad
ZO-1
bacteria
F-actin
E-cad
ZO-1
Overlay
E
cell nuclei / bacteria
F-actin / E-cad / ZO-1
F
zoom
INSET
Transverse
Longitudinal
bacteria
F-actin
ZO-1
G
Transverse
Normalized Intensity (A.U.)
Distance (µm)
H
Longitudinal
Normalized Intensity (A.U.)
Distance (µm)
I
F-actin
ZO-1
bacteria
Normalized Intensity (A.U.)
Distance (µm)
J
Luminal Microbes
Nutrients
Bacteria
Continuous IMAC Barrier
Epithelium
Brush Border Intact
Disrupted IMAC

Figure 5. SFB actin-dependent attachments incorporate ZO-1 and are continuous with cell-cell junctions. (A) Whole mount SEM of Cdhr2$^{fl/fl}$ and Cdhr2$^{\Delta epi}$ ileum villi, boxed areas enlarged in zooms 1-4. Zooms highlight tissue morphology at the villus tips. (B) SEM of Cdhr2$^{\Delta epi}$ mouse terminal ileum highlighting discontinuity of microvilli packing at cell-cell junctions (transparent red overlay). (C) Quantification of the distance from the center of actin-dependent adherent bacteria to cell-cell junctions (Total F-Actin) and the subset of actin-dependent bacteria colocalized with EPS8 (F-Actin/EPS8). Each point on the graph represents one adherent bacterium; Total F-actin Cdhr2$^{fl/fl}$ n = 87, Cdhr2$^{\Delta epi}$ n = 148; F-Actin/EPS8 Cdhr2$^{fl/fl}$ n = 15, Cdhr2$^{\Delta epi}$ n = 39; representing bacteria from 4-6 mice for each genotype. Violin plots with a dotted line at the median. Significance calculated using the Mann-Whitney test, **** $p < 0.0001$. Median distance from the center of adherent bacteria to the nearest cell-cell junction of 1.56 µm v. 1.22 µm (Total F-actin) in Cdhr2$^{fl/fl}$ and Cdhr2$^{\Delta epi}$ villi respectively; median distance from the center of adherent bacteria to the nearest cell-cell junction 1.41 µm v. 0.99 µm (F-actin/EPS8) in Cdhr2$^{fl/fl}$ and Cdhr2$^{\Delta epi}$ villi respectively. (D) MaxIP (depth 1.6 µm) of Cdhr2$^{\Delta epi}$ ileum stained with DAPI (DNA), phalloidin (F-actin), E-cadherin, and ZO-1. DNA segmented using an AI algorithm to isolate bacterial DNA (yellow) from cell nuclei (blue). Boxed areas enlarged in zooms 1-3 show individual channels (bacteria, F-actin E-cadherin, ZO-1) and the overlay. (E) 3D volume from the upper left of (D) optically sectioned through a single adherent bacterial filament (D, zoom 3). The oblique section is parallel to the bacterial filament and perpendicular to the cell surface. Boxed area enlarged in F. (F) Oblique section through a single SFB attachment. Individual channels (bacteria, F-actin, and ZO-1) shown below. INSET indicates the Transverse and Longitudinal regions of interest analyzed in G and H. (G) Transverse fluorescence intensity distributions of F-actin, ZO-1, and bacteria of a representative adherent bacterial filament. Intensities measured at the surface extending across multiple cells (C1 = cell 1, C2 = cell 2, bact = adherent bacteria). (H) Longitudinal fluorescence intensity distributions of F-actin, ZO-1, and bacteria of a representative adherent bacterial filament. Intensities measured parallel to the bacterial filament/F-actin attachment extending from intracellular (IC) to extracellular (EC). (I) Longitudinal fluorescence intensity distributions of F-actin, ZO-1, and bacteria extending from intracellular to extracellular. Peak F-actin intensity set at 0. (J) Model of the impact of IMAC disruption on epithelial surface defense against luminal bacteria. Scale bars: 100 µm (A main panel), 20 µm (D), 10 µm (A, zooms 1-4), 5 µm (B; D, zooms 1-3), 2 µm (E-F).

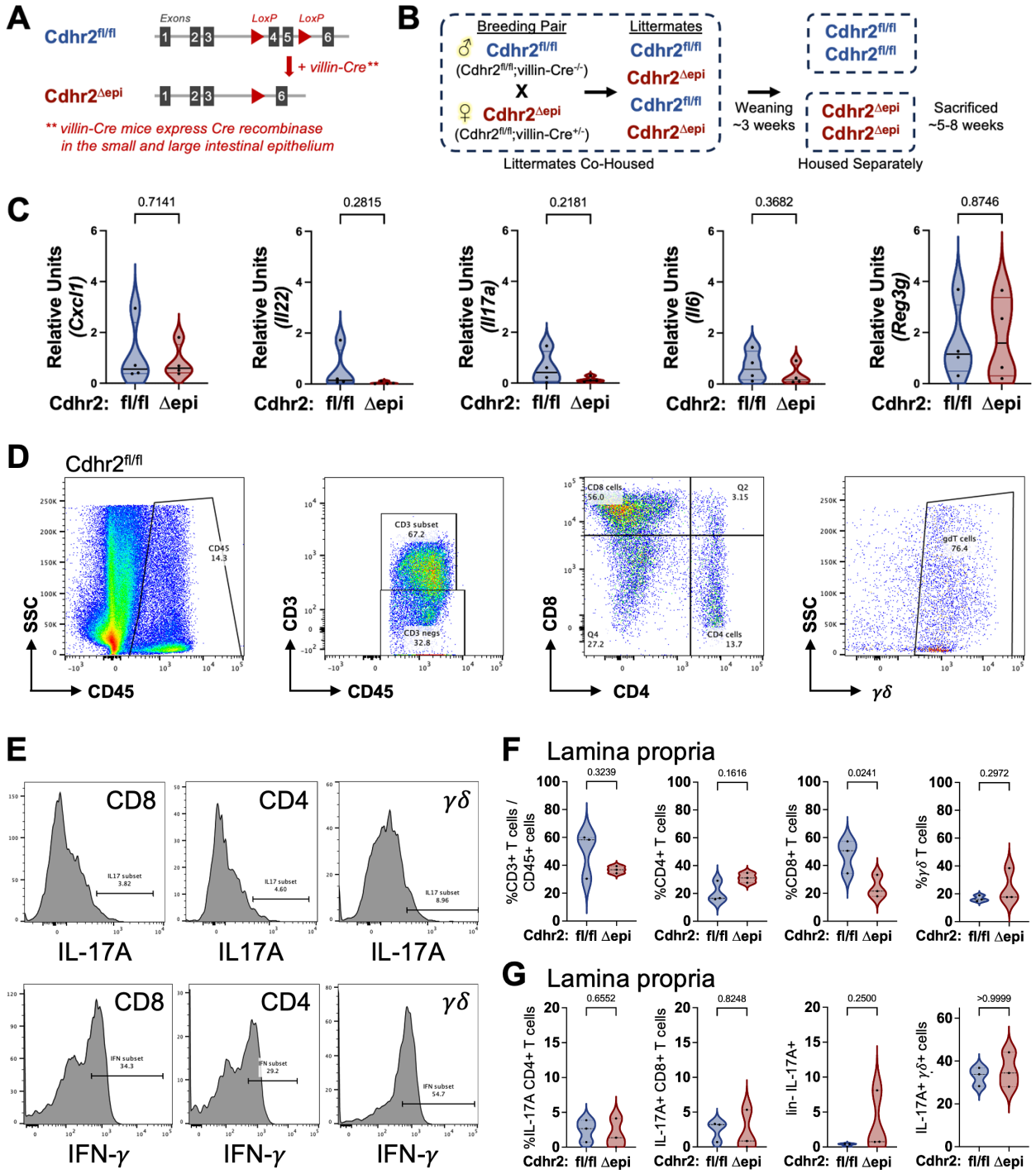

Supplemental Figure S1. Mice with a disrupted IMAC do not have increased inflammation. (A) Simplified diagram of the strategy used to generate *Cdhr2*$^{\Delta epi}$ mice from *Cdhr2*$^{fl/fl}$ in combination with tissue-specific expression of Cre; previously described in Pinette et al. 2019[35]. (B) Diagram of breeding strategy. Using a background of *Cdhr2*$^{fl/fl}$ mice, introduction of a single copy of villin-Cre (*villin-Cre*$^{+/-}$) in the mating pair results in a mixed litter of *Cdhr2*$^{fl/fl}$ and *Cdhr2*$^{\Delta epi}$ mice. (C) The expression of *Cxcl1, Il22,*

Il17A, Il6 and *Reg3g* in RNA extracted from the terminal ileum at 6-8 weeks of age was assessed by qRT-PCR. Relative units are calculated as described in the Materials and Methods, *Gapdh* was used as endogenous control. Statistical analysis performed using unpaired t-tests. Error bars represent mean ± SEM. (D-G) Flow cytometry analysis of T cells within the lamina propria in knockout C*dhr2*$^{\Delta epi}$ and control *Cdhr2*$^{fl/fl}$ mice. (D) Two-dimensional flow cytometry plots show the gating strategy of CD45^{+} immune cells in gastrointestinal tissue to identify CD3^{+} T cells within CD45^{+} immune cells, CD4^{+} and CD8^{+} T cells and $\gamma\delta$ T cells. (E) Histograms show gating strategy used to identify IL-17A and IFN-γ expressing cells in CD8^{+} T cells, CD4^{+} T cells, and $\gamma\delta$ T cells. (F) Violin plots show proportions of T cell populations in the lamina propria of matched *Cdhr2*$^{fl/fl}$ and *Cdhr2*$^{\Delta epi}$ mice (CD3^{+} T cells over total CD45^{+} T cells) and (CD4^{+} T cells, CD8^{+} T cells and $\gamma\delta$ T cells over total CD3^{+} T cells). (G) Violin plots show proportions of IL-17A expressing T cells (CD4, CD8), lineage negative and $\gamma\delta$ T cells, in the small intestine lamina propria of matched *Cdhr2*$^{fl/fl}$ and *Cdhr2*$^{\Delta epi}$ mice, n = 3. Statistical analysis performed using paired Wilcoxon test.

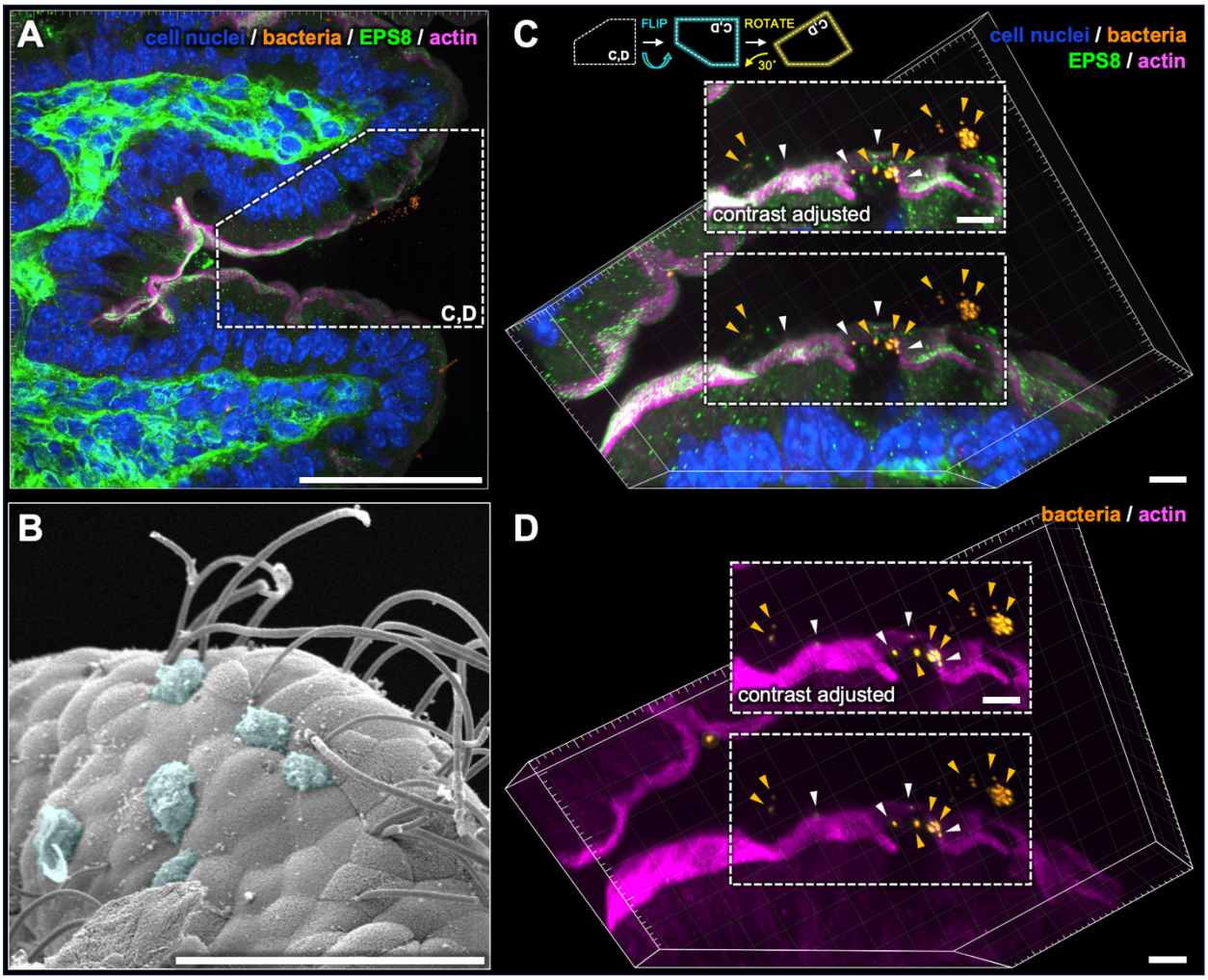

Supplemental Figure S2. Tissue-associated bacteria form actin-independent surface attachments—goblet cell and mucus binding. (A) Deconvolved confocal 3D image of *Cdhr2*$^{\Delta epi}$ ileum viewed as a maxIP (depth 11.25 µm) stained for DNA (DAPI), EPS8, and actin. DAPI segmented using an AI algorithm to isolate and differentially contrast bacteria (orange) relative to cell nuclei (blue). Boxed area enlarged and rotated in C and D. (B) SEM of *Cdhr2*$^{\Delta epi}$ ileum. Retained mucus highlighted by transparent cyan overlay. (C) Boxed area from (A) with cell nuclei, bacteria, EPS8, and actin; cropped, enlarged, contrast enhanced, and positioned (flipped vertically, rotated ~30˚ counterclockwise, tilted) to optimize visualization of bacteria relative to the cell surface. Arrowheads highlight bacteria in contact with goblet cells (white) or the adjacent lumen (orange). Boxed area in shown above with augmented brightness/contrast to visualize dim signals. (D) Boxed area from (A) showing only the bacteria and actin channels; cropped, enlarged, contrast enhanced, and positioned (flipped vertically, rotated ~30˚ counterclockwise, tilted) to optimize visualization of bacteria. Arrowheads highlight bacteria in contact with goblet cells (white) or in the adjacent lumen (orange). Boxed area in shown above with augmented brightness/contrast to visualize dim signals. Scale bars: 50 µm (A, B), 5 µm (C, D).

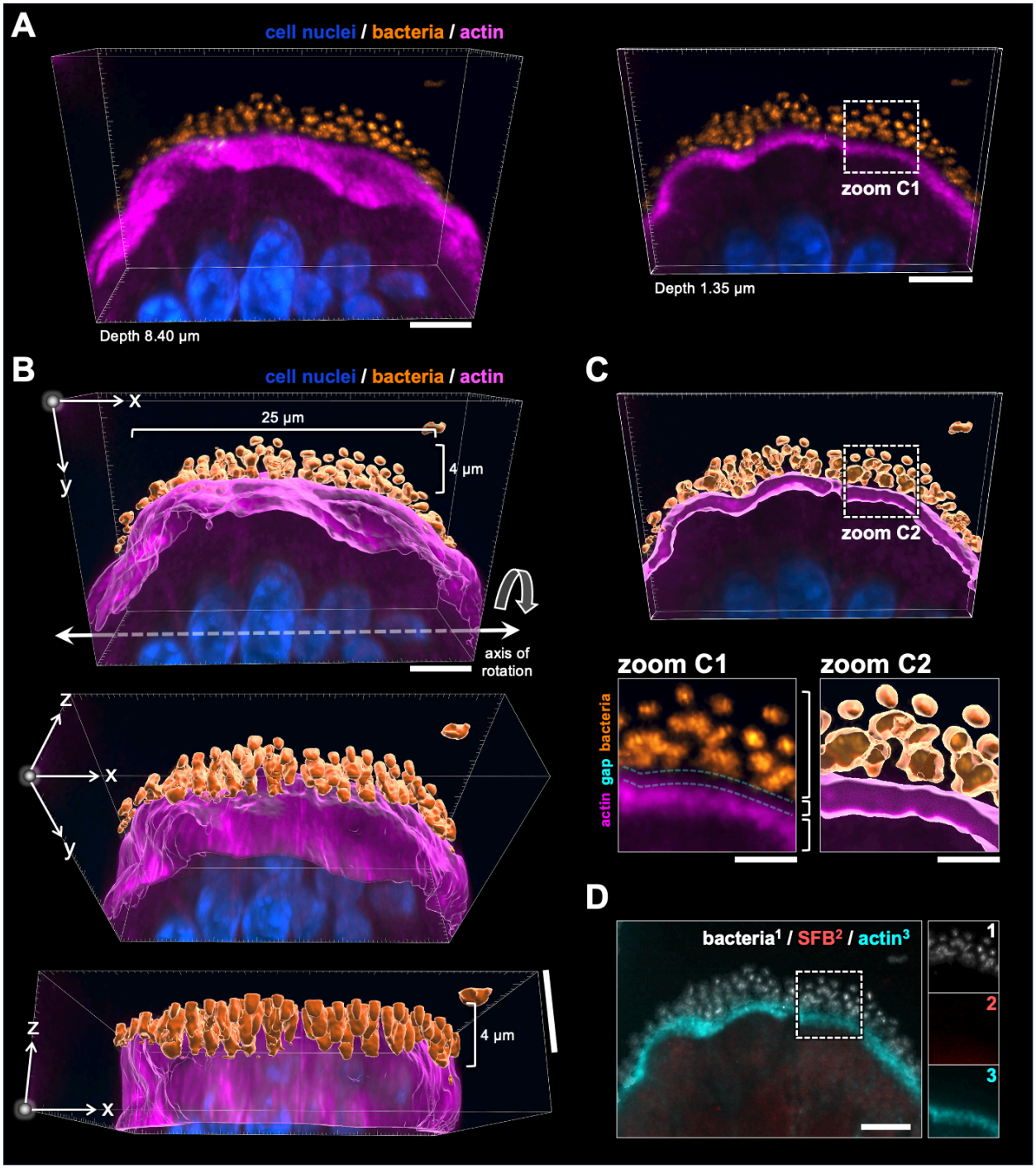

Supplemental Figure S3. Mucosal bacteria form layered three-dimensional structures that are actin-independent. (A) Villus tip from Cdhr2$^{\Delta epi}$ ileum (Figure 3J, zoom 1) viewed as a MaxIP (depth 8.40 µm, left; depth 1.35 µm, right) and rendered in 3D. Tissue stained with DAPI (DNA) and for actin. DAPI segmented using an AI algorithm to isolate and differentially contrast bacterial DNA (orange) relative to cell nuclei (blue). Boxed area enlarged in zoom C1. (B) MaxIP (depth 8.40 µm) from (A) processed using Imaris to create a 3D surface from the fluorescent actin and bacteria

DNA signals. The surface is overlaid on the fluorescence image, then sequentially rotated around the x-axis to highlight the 3D composition of the bacteria overlying the F-actin surface. (C) MaxIP (depth 1.35 μm) from viewed as a surface to highlight the relationship between the bacteria and surface actin. Boxed area enlarged and contrast enhanced in zoom C2. Zooms C1-2 show enlarged images of the original fluorescence intensity (C1) and generated surface (C2) with a clear gap between the bacteria fluorescence and surface actin and continuity of the actin surface. (D) MaxIP (depth 1.35 μm) corresponding to the image volume in (A, right) with segmented DNA (bacteria), SFB FISH (SFB), and actin. Boxed area shown as separate channels (right). Scale bars: 5 μm (A-D), 2 μm (zoom C1-2).

REFERENCES

1. Krndija, D. *et al.* Active cell migration is critical for steady-state epithelial turnover in the gut. *Science* **365**, 705–710 (2019).
2. van der Flier, L.G. & Clevers, H. Stem cells, self-renewal, and differentiation in the intestinal epithelium. *Annu Rev Physiol* **71**, 241–260 (2009).
3. Weck, M.L., Crawley, S.W. & Tyska, M.J. A heterologous in-cell assay for investigating intermicrovillar adhesion complex interactions reveals a novel protrusion length-matching mechanism. *J Biol Chem* **295**, 16191–16206 (2020).
4. Crawley, S.W. *et al.* Intestinal brush border assembly driven by protocadherin-based intermicrovillar adhesion. *Cell* **157**, 433–446 (2014).
5. Dyduch, A., Karczewska, K., Grzybek, H. & Kamiński, M. Transmission electron microscopy of microvilli of intestinal epithelial cells in celiac disease in remission and transient gluten enteropathy in children after a gluten-free diet. *J Pediatr Gastroenterol Nutr* **16**, 269–272 (1993).
6. VanDussen, K.L. *et al.* Abnormal Small Intestinal Epithelial Microvilli in Patients With Crohn's Disease. *Gastroenterology* **155**, 815–828 (2018).
7. Abraham, C. & Cho, J.H. Inflammatory bowel disease. *N Engl J Med* **361**, 2066–2078 (2009).
8. Sharma, B. *et al.* Gut Microbiota Serves as a Crucial Independent Biomarker in Inflammatory Bowel Disease (IBD). *Int J Mol Sci* **26** (2025).
9. Osterman, M.T. *et al.* Epithelial Cell Biomarkers Are Predictive of Response to Biologic Agents in Crohn's Disease. *Inflamm Bowel Dis* **27**, 677–685 (2021).
10. Mooseker, M.S. & Tilney, L.G. Organization of an actin filament-membrane complex. Filament polarity and membrane attachment in the microvilli of intestinal epithelial cells. *J Cell Biol* **67**, 725–743 (1975).
11. Ohta, K., Higashi, R., Sawaguchi, A. & Nakamura, K. Helical arrangement of filaments in microvillar actin bundles. *J Struct Biol* **177**, 513–519 (2012).
12. Meenderink, L.M. *et al.* Actin Dynamics Drive Microvillar Motility and Clustering during Brush Border Assembly. *Dev Cell* **50**, 545–556.e544 (2019).
13. Chinowsky, C.R., Pinette, J.A., Meenderink, L.M., Lau, K.S. & Tyska, M.J. Nonmuscle myosin-2 contractility-dependent actin turnover limits the length of epithelial microvilli. *Mol Biol Cell* **31**, 2803–2815 (2020).
14. Ebrahim, S. *et al.* NMII forms a contractile transcellular sarcomeric network to regulate apical cell junctions and tissue geometry. *Curr Biol* **23**, 731–736 (2013).
15. Tilney, L.G. & Cardell, R.R. Factors controlling the reassembly of the microvillous border of the small intestine of the salamander. *J Cell Biol* **47**, 408–422 (1970).
16. Hertzog, M. *et al.* Molecular basis for the dual function of Eps8 on actin dynamics: bundling and capping. *PLoS Biol* **8**, e1000387 (2010).
17. Gaeta, I.M., Meenderink, L.M., Postema, M.M., Cencer, C.S. & Tyska, M.J. Direct visualization of epithelial microvilli biogenesis. *Curr Biol* **31**, 2561–2575.e2566 (2021).
18. Postema, M.M., Grega-Larson, N.E., Neininger, A.C. & Tyska, M.J. IRTKS (BAIAP2L1) Elongates Epithelial Microvilli Using EPS8-Dependent and Independent Mechanisms. *Curr Biol* **28**, 2876–2888.e2874 (2018).

19. Bretscher, A. & Weber, K. Villin: the major microfilament-associated protein of the intestinal microvillus. *Proc Natl Acad Sci U S A* **76**, 2321–2325 (1979).
20. Bartles, J.R., Zheng, L., Li, A., Wierda, A. & Chen, B. Small espin: a third actin-bundling protein and potential forked protein ortholog in brush border microvilli. *J Cell Biol* **143**, 107–119 (1998).
21. Bretscher, A. & Weber, K. Fimbrin, a new microfilament-associated protein present in microvilli and other cell surface structures. *J Cell Biol* **86**, 335–340 (1980).
22. Morales, E.A., Arnaiz, C., Krystofiak, E.S., Zanic, M. & Tyska, M.J. Mitotic Spindle Positioning (MISP) is an actin bundler that selectively stabilizes the rootlets of epithelial microvilli. *Cell Rep* **39**, 110692 (2022).
23. Tyska, M.J. *et al.* Myosin-1a is critical for normal brush border structure and composition. *Mol Biol Cell* **16**, 2443–2457 (2005).
24. Benesh, A.E. *et al.* Differential localization and dynamics of class I myosins in the enterocyte microvillus. *Mol Biol Cell* **21**, 970–978 (2010).
25. Hegan, P.S., Giral, H., Levi, M. & Mooseker, M.S. Myosin VI is required for maintenance of brush border structure, composition, and membrane trafficking functions in the intestinal epithelial cell. *Cytoskeleton (Hoboken)* **69**, 235–251 (2012).
26. Casaletto, J.B., Saotome, I., Curto, M. & McClatchey, A.I. Ezrin-mediated apical integrity is required for intestinal homeostasis. *Proc Natl Acad Sci U S A* **108**, 11924–11929 (2011).
27. Hartmann, C. *et al.* Intestinal brush border formation requires a TMIGD1-based intermicrovillar adhesion complex. *Sci Signal* **15**, eabm2449 (2022).
28. Crawley, S.W., Weck, M.L., Grega-Larson, N.E., Shifrin, D.A., Jr. & Tyska, M.J. ANKS4B Is Essential for Intermicrovillar Adhesion Complex Formation. *Dev Cell* **36**, 190–200 (2016).
29. Li, J., He, Y., Lu, Q. & Zhang, M. Mechanistic Basis of Organization of the Harmonin/USH1C-Mediated Brush Border Microvilli Tip-Link Complex. *Developmental cell* **36**, 179–189 (2016).
30. Li, J. *et al.* Structure of Myo7b/USH1C complex suggests a general PDZ domain binding mode by MyTH4-FERM myosins. *Proceedings of the National Academy of Sciences of the United States of America* **114**, E3776–e3785 (2017).
31. Yu, I.M. *et al.* Myosin 7 and its adaptors link cadherins to actin. *Nat Commun* **8**, 15864 (2017).
32. Choi, M.S. *et al.* The small EF-hand protein CALML4 functions as a critical myosin light chain within the intermicrovillar adhesion complex. *J Biol Chem* **295**, 9281–9296 (2020).
33. Weck, M.L., Crawley, S.W., Stone, C.R. & Tyska, M.J. Myosin-7b Promotes Distal Tip Localization of the Intermicrovillar Adhesion Complex. *Curr Biol* **26**, 2717–2728 (2016).
34. Cencer, C.S. *et al.* Adhesion-based capture stabilizes nascent microvilli at epithelial cell junctions. *Dev Cell* **58**, 2048–2062.e2047 (2023).
35. Pinette, J.A. *et al.* Brush border protocadherin CDHR2 promotes the elongation and maximized packing of microvilli in vivo. *Mol Biol Cell* **30**, 108–118 (2019).

36. Mödl, B. *et al.* Defects in microvillus crosslinking sensitize to colitis and inflammatory bowel disease. *EMBO Rep* **24**, e57084 (2023).
37. Cencer, C.S., Robinson, K.L. & Tyska, M.J. Loss of intermicrovillar adhesion factor CDHR2 impairs basolateral junctional complexes in transporting epithelia. *Mol Biol Cell* **35**, br21 (2024).
38. Revenu, C. *et al.* A new role for the architecture of microvillar actin bundles in apical retention of membrane proteins. *Mol Biol Cell* **23**, 324–336 (2012).
39. Grimm-Günter, E.M. *et al.* Plastin 1 binds to keratin and is required for terminal web assembly in the intestinal epithelium. *Mol Biol Cell* **20**, 2549–2562 (2009).
40. Ferrary, E. *et al.* In vivo, villin is required for Ca(2+)-dependent F-actin disruption in intestinal brush borders. *J Cell Biol* **146**, 819–830 (1999).
41. Peterson, L.W. & Artis, D. Intestinal epithelial cells: regulators of barrier function and immune homeostasis. *Nat Rev Immunol* **14**, 141–153 (2014).
42. Yu, L.C. Commensal bacterial internalization by epithelial cells: An alternative portal for gut leakiness. *Tissue Barriers* **3**, e1008895 (2015).
43. Tilney, L.G. & Portnoy, D.A. Actin filaments and the growth, movement, and spread of the intracellular bacterial parasite, Listeria monocytogenes. *J Cell Biol* **109**, 1597–1608 (1989).
44. Tilney, L.G., Connelly, P.S. & Portnoy, D.A. Actin filament nucleation by the bacterial pathogen, Listeria monocytogenes. *J Cell Biol* **111**, 2979–2988 (1990).
45. Tilney, L.G., DeRosier, D.J. & Tilney, M.S. How Listeria exploits host cell actin to form its own cytoskeleton. I. Formation of a tail and how that tail might be involved in movement. *J Cell Biol* **118**, 71–81 (1992).
46. Tilney, L.G., DeRosier, D.J., Weber, A. & Tilney, M.S. How Listeria exploits host cell actin to form its own cytoskeleton. II. Nucleation, actin filament polarity, filament assembly, and evidence for a pointed end capper. *J Cell Biol* **118**, 83–93 (1992).
47. Pistor, S., Chakraborty, T., Niebuhr, K., Domann, E. & Wehland, J. The ActA protein of Listeria monocytogenes acts as a nucleator inducing reorganization of the actin cytoskeleton. *Embo j* **13**, 758–763 (1994).
48. Naydenov, N.G., Marino-Melendez, A., Campellone, K.G. & Ivanov, A.I. Cytoskeletal mechanisms regulating attaching/effacing bacteria interactions with host cells: It takes a village to build the pedestal. *Bioessays* **46**, e2400160 (2024).
49. Finlay, B.B. & Falkow, S. Salmonella interactions with polarized human intestinal Caco-2 epithelial cells. *J Infect Dis* **162**, 1096–1106 (1990).
50. Ly, K.T. & Casanova, J.E. Mechanisms of Salmonella entry into host cells. *Cell Microbiol* **9**, 2103–2111 (2007).
51. Zhou, D., Mooseker, M.S. & Galán, J.E. An invasion-associated Salmonella protein modulates the actin-bundling activity of plastin. *Proc Natl Acad Sci U S A* **96**, 10176–10181 (1999).
52. Zhou, D., Mooseker, M.S. & Galán, J.E. Role of the S. typhimurium actin-binding protein SipA in bacterial internalization. *Science* **283**, 2092–2095 (1999).
53. Hayward, R.D. & Koronakis, V. Direct nucleation and bundling of actin by the SipC protein of invasive Salmonella. *Embo j* **18**, 4926–4934 (1999).

54. Pollock, G.L. *et al.* Targeting of microvillus protein Eps8 by the NleH effector kinases from enteropathogenic E. coli. *Proc Natl Acad Sci U S A* **119**, e2204332119 (2022).
55. Shifrin, D.A., Jr., Crawley, S.W., Grega-Larson, N.E. & Tyska, M.J. Dynamics of brush border remodeling induced by enteropathogenic E. coli. *Gut Microbes* **5**, 504–516 (2014).
56. Hardt, W.D., Chen, L.M., Schuebel, K.E., Bustelo, X.R. & Galán, J.E. S. typhimurium encodes an activator of Rho GTPases that induces membrane ruffling and nuclear responses in host cells. *Cell* **93**, 815–826 (1998).
57. Fu, Y. & Galán, J.E. The Salmonella typhimurium tyrosine phosphatase SptP is translocated into host cells and disrupts the actin cytoskeleton. *Mol Microbiol* **27**, 359–368 (1998).
58. Caron, E. *et al.* Subversion of actin dynamics by EPEC and EHEC. *Curr Opin Microbiol* **9**, 40–45 (2006).
59. Velle, K.B. & Campellone, K.G. Enteropathogenic E. coli relies on collaboration between the formin mDia1 and the Arp2/3 complex for actin pedestal biogenesis and maintenance. *PLOS Pathogens* **14**, e1007485 (2018).
60. Croce, A. *et al.* A novel actin barbed-end-capping activity in EPS-8 regulates apical morphogenesis in intestinal cells of Caenorhabditis elegans. *Nat Cell Biol* **6**, 1173–1179 (2004).
61. Disanza, A. *et al.* Eps8 controls actin-based motility by capping the barbed ends of actin filaments. *Nat Cell Biol* **6**, 1180–1188 (2004).
62. Jiang, H.Q., Bos, N.A. & Cebra, J.J. Timing, localization, and persistence of colonization by segmented filamentous bacteria in the neonatal mouse gut depend on immune status of mothers and pups. *Infect Immun* **69**, 3611–3617 (2001).
63. Klaasen, H.L., Koopman, J.P., Poelma, F.G. & Beynen, A.C. Intestinal, segmented, filamentous bacteria. *FEMS Microbiol Rev* **8**, 165–180 (1992).
64. Croswell, A., Amir, E., Teggatz, P., Barman, M. & Salzman, N.H. Prolonged impact of antibiotics on intestinal microbial ecology and susceptibility to enteric Salmonella infection. *Infect Immun* **77**, 2741–2753 (2009).
65. Snel, J. *et al.* Comparison of 16S rRNA sequences of segmented filamentous bacteria isolated from mice, rats, and chickens and proposal of "Candidatus Arthromitus". *Int J Syst Bacteriol* **45**, 780–782 (1995).
66. Salzman, N.H. *et al.* Enteric defensins are essential regulators of intestinal microbial ecology. *Nat Immunol* **11**, 76–83 (2010).
67. Sengupta, R. *et al.* The role of cell surface architecture of lactobacilli in host-microbe interactions in the gastrointestinal tract. *Mediators Inflamm* **2013**, 237921 (2013).
68. Zheng, Y. *et al.* Mutual adhesion of Lactobacillus spp. to intestinal cells: A review of perspectives on surface layer proteins and cell surface receptors. *Int J Biol Macromol* **282**, 137031 (2024).
69. Chase, D.G. & Erlandsen, S.L. Evidence for a complex life cycle and endospore formation in the attached, filamentous, segmented bacterium from murine ileum. *J Bacteriol* **127**, 572–583 (1976).

70. Millard, T.H., Dawson, J. & Machesky, L.M. Characterisation of IRTKS, a novel IRSp53/MIM family actin regulator with distinct filament bundling properties. *J Cell Sci* **120**, 1663–1672 (2007).
71. Ahmed, S., Goh, W.I. & Bu, W. I-BAR domains, IRSp53 and filopodium formation. *Semin Cell Dev Biol* **21**, 350–356 (2010).
72. Zhao, H., Pykäläinen, A. & Lappalainen, P. I-BAR domain proteins: linking actin and plasma membrane dynamics. *Curr Opin Cell Biol* **23**, 14–21 (2011).
73. Yamagishi, A., Masuda, M., Ohki, T., Onishi, H. & Mochizuki, N. A novel actin bundling/filopodium-forming domain conserved in insulin receptor tyrosine kinase substrate p53 and missing in metastasis protein. *J Biol Chem* **279**, 14929–14936 (2004).
74. Amann, K.J. & Pollard, T.D. The Arp2/3 complex nucleates actin filament branches from the sides of pre-existing filaments. *Nat Cell Biol* **3**, 306–310 (2001).
75. Jepson, M.A., Clark, M.A., Simmons, N.L. & Hirst, B.H. Actin accumulation at sites of attachment of indigenous apathogenic segmented filamentous bacteria to mouse ileal epithelial cells. *Infect Immun* **61**, 4001–4004 (1993).
76. Hansson, G.C. & Johansson, M.E. The inner of the two Muc2 mucin-dependent mucus layers in colon is devoid of bacteria. *Gut Microbes* **1**, 51–54 (2010).
77. Johansson, M.E. *et al.* The inner of the two Muc2 mucin-dependent mucus layers in colon is devoid of bacteria. *Proc Natl Acad Sci U S A* **105**, 15064–15069 (2008).
78. Johansson, M.E. *et al.* Bacteria penetrate the inner mucus layer before inflammation in the dextran sulfate colitis model. *PLoS One* **5**, e12238 (2010).
79. Johansson, M.E. *et al.* Bacteria penetrate the normally impenetrable inner colon mucus layer in both murine colitis models and patients with ulcerative colitis. *Gut* **63**, 281–291 (2014).
80. Schneider, H., Pelaseyed, T., Svensson, F. & Johansson, M.E.V. Study of mucin turnover in the small intestine by in vivo labeling. *Sci Rep* **8**, 5760 (2018).
81. Boyle, E.C. & Finlay, B.B. Bacterial pathogenesis: exploiting cellular adherence. *Curr Opin Cell Biol* **15**, 633–639 (2003).
82. Pizarro-Cerdá, J. & Cossart, P. Bacterial adhesion and entry into host cells. *Cell* **124**, 715–727 (2006).
83. Kirjavainen, P.V., Ouwehand, A.C., Isolauri, E. & Salminen, S.J. The ability of probiotic bacteria to bind to human intestinal mucus. *FEMS Microbiol Lett* **167**, 185–189 (1998).
84. Johansson, M.E., Sjövall, H. & Hansson, G.C. The gastrointestinal mucus system in health and disease. *Nat Rev Gastroenterol Hepatol* **10**, 352–361 (2013).
85. Ouwerkerk, J.P., de Vos, W.M. & Belzer, C. Glycobiome: bacteria and mucus at the epithelial interface. *Best Pract Res Clin Gastroenterol* **27**, 25–38 (2013).
86. Rossi, E. *et al.* "It's a gut feeling" - Escherichia coli biofilm formation in the gastrointestinal tract environment. *Crit Rev Microbiol* **44**, 1–30 (2018).
87. Poceviciute, R. *et al.* Quantitative whole-tissue 3D imaging reveals bacteria in close association with mouse jejunum mucosa. *NPJ Biofilms Microbiomes* **9**, 64 (2023).

88. van der Waaij, L.A. *et al.* Bacterial population analysis of human colon and terminal ileum biopsies with 16S rRNA-based fluorescent probes: commensal bacteria live in suspension and have no direct contact with epithelial cells. *Inflamm Bowel Dis* **11**, 865–871 (2005).
89. DeGruttola, A.K., Low, D., Mizoguchi, A. & Mizoguchi, E. Current Understanding of Dysbiosis in Disease in Human and Animal Models. *Inflamm Bowel Dis* **22**, 1137–1150 (2016).
90. Kastl, A.J., Jr., Terry, N.A., Wu, G.D. & Albenberg, L.G. The Structure and Function of the Human Small Intestinal Microbiota: Current Understanding and Future Directions. *Cell Mol Gastroenterol Hepatol* **9**, 33–45 (2020).
91. Steinbach, E. *et al.* Upper small intestine microbiome in obesity and related metabolic disorders: A new field of investigation. *Metabolism* **150**, 155712 (2024).
92. Assa, A. *et al.* Mucosa-Associated Ileal Microbiota in New-Onset Pediatric Crohn's Disease. *Inflamm Bowel Dis* **22**, 1533–1539 (2016).
93. He, C. *et al.* Characteristics of mucosa-associated gut microbiota during treatment in Crohn's disease. *World J Gastroenterol* **25**, 2204–2216 (2019).
94. Yin, J. *et al.* Bacterial microbiome profiles of the inflamed terminal ileum mucosa in active Crohn's disease patients. *PeerJ* **13**, e19959 (2025).
95. Girbovan, A., Sur, G., Samasca, G. & Lupan, I. Dysbiosis a risk factor for celiac disease. *Med Microbiol Immunol* **206**, 83–91 (2017).
96. Norkina, O., Burnett, T.G. & De Lisle, R.C. Bacterial overgrowth in the cystic fibrosis transmembrane conductance regulator null mouse small intestine. *Infect Immun* **72**, 6040–6049 (2004).
97. Sovran, B. *et al.* Age-associated Impairment of the Mucus Barrier Function is Associated with Profound Changes in Microbiota and Immunity. *Sci Rep* **9**, 1437 (2019).
98. Tomas, J. *et al.* High-fat diet modifies the PPAR-γ pathway leading to disruption of microbial and physiological ecosystem in murine small intestine. *Proc Natl Acad Sci U S A* **113**, E5934–e5943 (2016).
99. Brown, E.M. *et al.* Diet and specific microbial exposure trigger features of environmental enteropathy in a novel murine model. *Nat Commun* **6**, 7806 (2015).
100. Tipton, L., Darcy, J.L. & Hynson, N.A. A Developing Symbiosis: Enabling Cross-Talk Between Ecologists and Microbiome Scientists. *Front Microbiol* **10**, 292 (2019).
101. Berg, G. *et al.* Microbiome definition re-visited: old concepts and new challenges. *Microbiome* **8**, 103 (2020).
102. Lee, J.Y., Bays, D.J., Savage, H.P. & Bäumler, A.J. The human gut microbiome in health and disease: time for a new chapter? *Infect Immun* **92**, e0030224 (2024).
103. Klaasen, H.L. *et al.* Apathogenic, intestinal, segmented, filamentous bacteria stimulate the mucosal immune system of mice. *Infect Immun* **61**, 303–306 (1993).

104. Ferguson, D.J. & Birch-Andersen, A. Electron microscopy of a filamentous, segmented bacterium attached to the small intestine of mice from a laboratory animal colony in Denmark. *Acta Pathol Microbiol Scand B* **87**, 247–252 (1979).
105. Brieher, W.M., Coughlin, M. & Mitchison, T.J. Fascin-mediated propulsion of Listeria monocytogenes independent of frequent nucleation by the Arp2/3 complex. *J Cell Biol* **165**, 233–242 (2004).
106. Kuwahara, T. *et al.* The lifestyle of the segmented filamentous bacterium: a non-culturable gut-associated immunostimulating microbe inferred by whole-genome sequencing. *DNA Res* **18**, 291–303 (2011).
107. Nkamba, I. *et al.* Intracellular offspring released from SFB filaments are flagellated. *Nat Microbiol* **5**, 34–39 (2020).
108. Ladinsky, M.S. *et al.* Endocytosis of commensal antigens by intestinal epithelial cells regulates mucosal T cell homeostasis. *Science* **363** (2019).
109. Davis, C.P. & Savage, D.C. Habitat, succession, attachment, and morphology of segmented, filamentous microbes indigenous to the murine gastrointestinal tract. *Infect Immun* **10**, 948–956 (1974).
110. Erlandsen, S.L. & Chase, D.G. Morphological alterations in the microvillous border of villous epithelial cells produced by intestinal microorganisms. *Am J Clin Nutr* **27**, 1277–1286 (1974).
111. Reimann, H.A. MICROBIC PHAGOCYTOSIS BY ENTERIC EPITHELIAL CELLS. *Jama* **192**, 1130–1132 (1965).
112. Maroux, S., Coudrier, E., Feracci, H., Gorvel, J.P. & Louvard, D. Molecular organization of the intestinal brush border. *Biochimie* **70**, 1297–1306 (1988).
113. Tocchetti, A. *et al.* Loss of the actin remodeler Eps8 causes intestinal defects and improved metabolic status in mice. *PLoS One* **5**, e9468 (2010).
114. Tyska, M.J. & Mooseker, M.S. MYO1A (brush border myosin I) dynamics in the brush border of LLC-PK1-CL4 cells. *Biophys J* **82**, 1869–1883 (2002).
115. Henderson, J.M. *et al.* Tunnelling nanotube formation is driven by Eps8/IRSp53-dependent linear actin polymerization. *Embo j* **42**, e113761 (2023).
116. Lie, P.P., Mruk, D.D., Lee, W.M. & Cheng, C.Y. Epidermal growth factor receptor pathway substrate 8 (Eps8) is a novel regulator of cell adhesion and the blood-testis barrier integrity in the seminiferous epithelium. *Faseb j* **23**, 2555–2567 (2009).
117. Cheng, C.Y. & Mruk, D.D. Regulation of spermiogenesis, spermiation and blood-testis barrier dynamics: novel insights from studies on Eps8 and Arp3. *Biochem J* **435**, 553–562 (2011).
118. Zimmerman, T.J. & Carabeo, R.A. Chlamydia trachomatis invasion: a duet of effectors. *Biochem Soc Trans* **0**, 363–370 (2025).
119. Dolat, L. *et al.* Chlamydia repurposes the actin-binding protein EPS8 to disassemble epithelial tight junctions and promote infection. *Cell Host Microbe* **30**, 1685–1700.e1610 (2022).
120. Stamatovic, S.M., Johnson, A.M., Sladojevic, N., Keep, R.F. & Andjelkovic, A.V. Endocytosis of tight junction proteins and the regulation of degradation and recycling. *Ann N Y Acad Sci* **1397**, 54–65 (2017).
121. Li, N., Mruk, D.D. & Cheng, C.Y. Actin binding proteins in blood-testis barrier function. *Curr Opin Endocrinol Diabetes Obes* **22**, 238–247 (2015).

122. Klaasen, H.L. *et al.* Intestinal, segmented, filamentous bacteria in a wide range of vertebrate species. *Lab Anim* **27**, 141–150 (1993).
123. Jonsson, H., Hugerth, L.W., Sundh, J., Lundin, E. & Andersson, A.F. Genome sequence of segmented filamentous bacteria present in the human intestine. *Commun Biol* **3**, 485 (2020).
124. Chen, H. *et al.* Distribution and Strain Diversity of Immunoregulating Segmented Filamentous Bacteria in Human Intestinal Lavage Samples. *Microb Ecol* **79**, 1021–1033 (2020).
125. Finotti, A. *et al.* PCR detection of segmented filamentous bacteria in the terminal ileum of patients with ulcerative colitis. *BMJ Open Gastroenterol* **4**, e000172 (2017).
126. Caselli, M., Tosini, D., Gafà, R., Gasbarrini, A. & Lanza, G. Segmented filamentous bacteria-like organisms in histological slides of ileo-cecal valves in patients with ulcerative colitis. *Am J Gastroenterol* **108**, 860–861 (2013).
127. Nowrouzian, F.L., Stadler, L.S., Adlerberth, I. & Wold, A.E. The 16S rRNA gene-based PCR method used for the detection of segmented filamentous bacteria in the intestinal microbiota generates false-positive results. *Apmis* **125**, 940–942 (2017).
128. Prakash, T. *et al.* Complete genome sequences of rat and mouse segmented filamentous bacteria, a potent inducer of th17 cell differentiation. *Cell Host Microbe* **10**, 273–284 (2011).
129. Sczesnak, A. *et al.* The genome of th17 cell-inducing segmented filamentous bacteria reveals extensive auxotrophy and adaptations to the intestinal environment. *Cell Host Microbe* **10**, 260–272 (2011).
130. Pamp, S.J., Harrington, E.D., Quake, S.R., Relman, D.A. & Blainey, P.C. Single-cell sequencing provides clues about the host interactions of segmented filamentous bacteria (SFB). *Genome Res* **22**, 1107–1119 (2012).
131. Schnupf, P., Gaboriau-Routhiau, V. & Cerf-Bensussan, N. Host interactions with Segmented Filamentous Bacteria: an unusual trade-off that drives the post-natal maturation of the gut immune system. *Semin Immunol* **25**, 342–351 (2013).
132. Schnupf, P. *et al.* Growth and host interaction of mouse segmented filamentous bacteria in vitro. *Nature* **520**, 99–103 (2015).
133. Liu, C. *et al.* Enlightening the taxonomy darkness of human gut microbiomes with a cultured biobank. *Microbiome* **9**, 119 (2021).
134. Browne, H.P. *et al.* Culturing of 'unculturable' human microbiota reveals novel taxa and extensive sporulation. *Nature* **533**, 543–546 (2016).
135. Nayfach, S., Shi, Z.J., Seshadri, R., Pollard, K.S. & Kyrpides, N.C. New insights from uncultivated genomes of the global human gut microbiome. *Nature* **568**, 505–510 (2019).
136. Atarashi, K. *et al.* Th17 Cell Induction by Adhesion of Microbes to Intestinal Epithelial Cells. *Cell* **163**, 367–380 (2015).
137. The Galaxy platform for accessible, reproducible, and collaborative data analyses: 2024 update. *Nucleic Acids Res* **52**, W83–w94 (2024).
138. Lu, J., Breitwieser, F.P., Thielen, P. & Salzberg, S.L. Bracken: estimating species abundance in metagenomics data. *PeerJ Comput Sci* **3** (2017).

139. Lu, J. *et al.* Metagenome analysis using the Kraken software suite. *Nat Protoc* **17**, 2815–2839 (2022).
140. Wang, G. *et al.* PyMIC: A deep learning toolkit for annotation-efficient medical image segmentation. *Comput Methods Programs Biomed* **231**, 107398 (2023).